Online Figure III

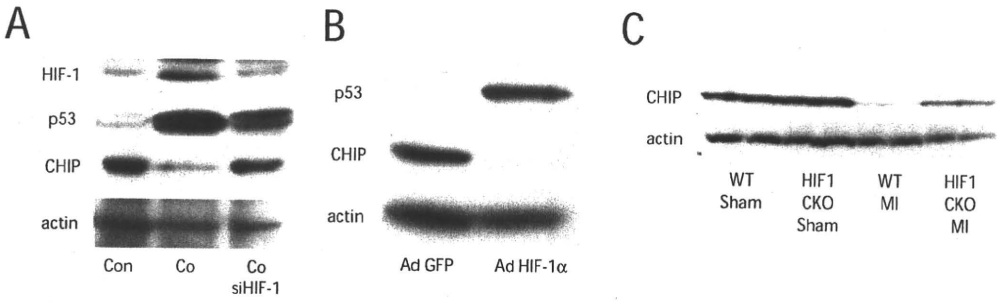

Online Figure IV

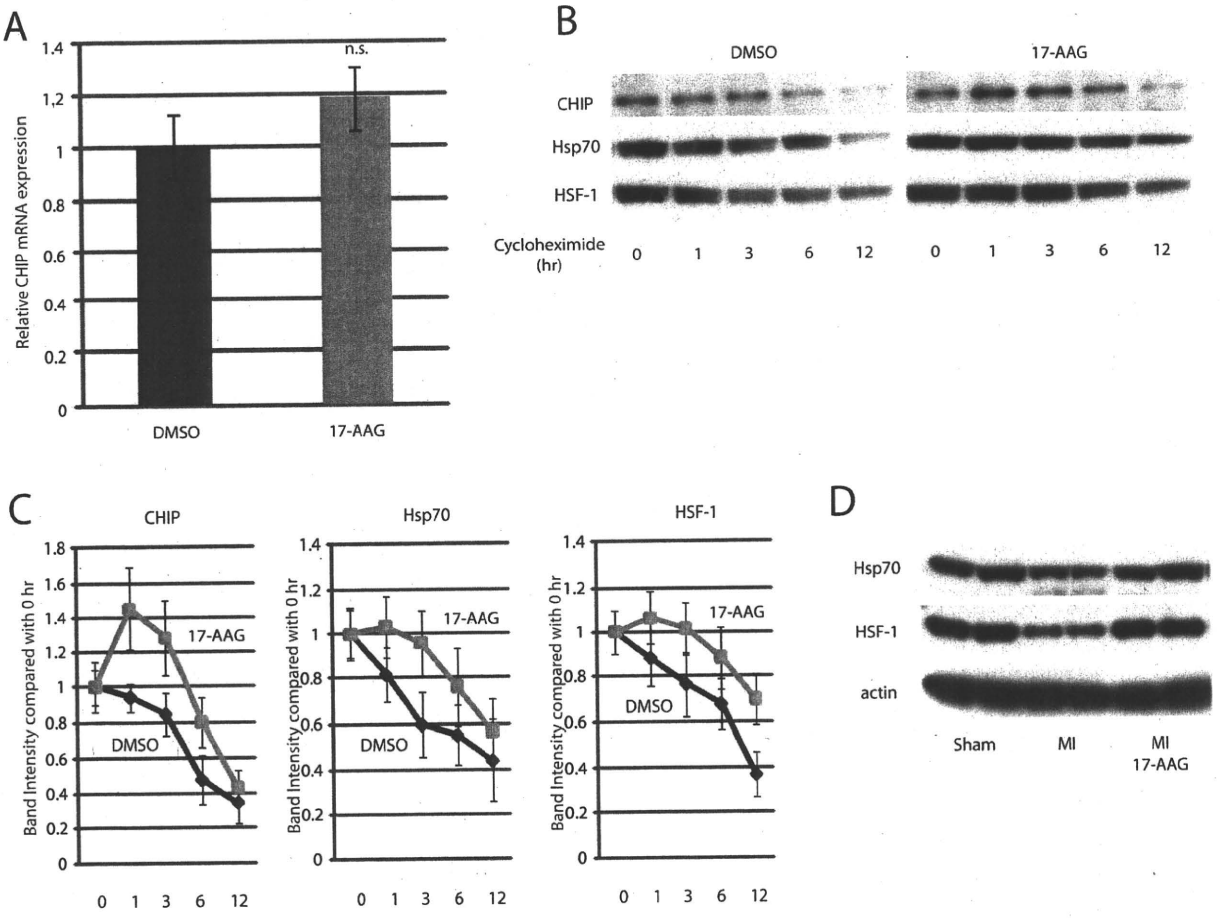

Figure Legends for Supplementary Figures

Online Figure I. (**A**) Tissue distribution of endogenous CHIP. (**B**) CHIP interacts with p53 in COS7 cells transfected with HA-CHIP and Flag-p53 as revealed by immunoprecipitation/western blot analysis. IP, immunoprecipitation. (**C**) Endogenous CHIP interacts with endogenous p53 in neonatal rat cardiomyocytes. (**D**) CHIP induces ubiquitination of p53 in cultured cardiomyocytes. Ubiquitinated p53 appears as a smear. MG132 was used as a positive control because it inhibits proteasomal degradation, leaving ubiquitinated protein undegraded. (**E**) MG132 prevents CHIP-induced p53 degradation in cultured cardiomyocytes. (**F**) Both $CoCl_2$ treatment and hypoxia induces p53 upregulation and CHIP downregulation in cardiomyocytes. Con, control; Co, $CoCl_2$. (**G**) HIF-1α activity was determined to confirm that HIF-1α was actually active by $CoCl_2$ treatment. Con, control; Co, $CoCl_2$.

Online Figure II. Densitometric analysis for the Western blot shown in Figure 2B. p53 protein level (**A**), and CHIP protein level (**B**).

Online Figure III. (**A**) Knockdown of HIF-1α by siRNA reverses the effect of $CoCl_2$ in cardiomyocytes. (**B**) Overexpression of HIF-1 downregulates CHIP expression and induces accumulation of p53 in cardiomyocytes. (**C**) Wild type and cardiac-specific inducible HIF-1α knockout mice were subjected to coronary artery ligation. HIF-1 deletion attenuates downregulation of CHIP expression induced by myocardial infarction. WT, wild type mice; CKO, cardiac-specific inducible HIF-1α knockout mice.

Online Figure IV. (**A**) 17-AAG treatment showed no effect on CHIP mRNA transcription. (**B**) Representative blots for the expression level of CHIP, Hsp70 and HSF-1 after treatment with cycloheximide 100 μg/mL, with or without 17-AAG. (**C**) Kinetics of protein stability obtained from densitometric analysis. (**D**) 17-AAG treatment

up-regulates the protein level of Hsp70 and HSF-1 after myocardial infarction.

THE JOURNAL OF BIOLOGICAL CHEMISTRY VOL. 285, NO. 49, pp. 38692–38699, December 3, 2010

Aggregation of Detergent-insoluble Tau Is Involved in Neuronal Loss but Not in Synaptic Loss*[S]

Received for publication, April 21, 2010, and in revised form, September 1, 2010 Published, JBC Papers in Press, October 4, 2010, DOI 10.1074/jbc.M110.136630

Tetsuya Kimura, Tetsuya Fukuda, Naruhiko Sahara, Shunji Yamashita, Miyuki Murayama, Tatsuya Mizoroki, Yuji Yoshiike, Boyoung Lee, Ioannis Sotiropoulos, Sumihiro Maeda, and Akihiko Takashima[1]

From the Laboratory for Alzheimer's Disease, Brain Science Institute, Riken, 2-1 Hirosawa, Wako, Saitama 351-0198, Japan

Neurofibrillary tangles (NFTs), which consist of highly phosphorylated tau, are hallmarks of neurodegenerative diseases including Alzheimer disease (AD). In neurodegenerative diseases, neuronal dysfunction due to neuronal loss and synaptic loss accompanies NFT formation, suggesting that a process associated with NFT formation may be involved in neuronal dysfunction. To clarify the relationship between the tau aggregation process and synapse and neuronal loss, we compared two lines of mice expressing human tau with or without an aggregation-prone P301L mutation. P301L tau transgenic (Tg) mice exhibited neuronal loss and produced sarcosyl-insoluble tau in old age but did not exhibit synaptic loss and memory impairment. By contrast, wild-type tau Tg mice neither exhibited neuronal loss nor produced sarcosyl-insoluble tau but did exhibit synaptic loss and memory impairment. Moreover, P301L tau was less phosphorylated than wild-type tau, suggesting that the tau phosphorylation state is involved in synaptic loss, whereas the tau aggregation state is involved in neuronal loss. Finally, increasing concentrations of insoluble tau aggregates leads to the formation of fibrillar tau, which causes NFTs to form.

NFTs[2] are commonly observed in neurodegenerative disorders. Brain regions containing NFTs also exhibit neuronal loss. The rate of neuron loss is much greater than the rate of NFT formation, suggesting that NFT formation and neuronal death share a common mechanism (1, 2). This hypothesis is strongly supported by the discovery of tau gene mutations in individuals with frontotemporal dementia with parkinsonism linked to chromosome 17 (FTDP-17) (3, 4). A single tau gene mutation induces NFT formation and neuronal loss with 100% penetration. Moreover, overexpression of human FTDP-17 tau induces NFT formation, neuronal loss, and behavioral deficits in mice (5–12).

Mice that overexpress P301L mutant tau under the regulation of a tetracycline-inducible promoter display age-related NFTs, neuronal death, and behavioral deficits (13, 14). Although inhibiting mutant tau overexpression in these mice blocks neuronal death and improves memory, NFTs continue to form (13, 15). This suggests that NFTs are not themselves toxic but, instead, that NFT formation and neuronal death and neuronal dysfunction share a common underlying mechanism.

The P301L tau mutation is known as an "aggregation-prone mutation" in that individuals harboring this mutation produce mutant tau that readily aggregates (16–18). The NFTs of one patient with an aggressive FTDP-17 phenotype consisted of only P301L mutant tau (19), indicating that P301L mutant tau itself may possess a toxic function by forming aggregated tau.

The formation of tau fibrils is believed to involve three sequential steps (20, 21). First, monomeric tau binds together to form oligomers that are soluble in sarcosyl solution. The structure of these oligomers, however, is not discernible under atomic force microscopy. Second, as soluble tau oligomers take on a β-sheet structure, they form tau aggregates that are insoluble in sarcosyl solution. These aggregates become granular-shaped oligomers consisting of ~40 tau molecules that are detectable under atomic force microscopy. Third, increasing concentrations of granular tau oligomer cause the oligomers to fuse to each other to form tau fibrils.

Prefrontal cortex displaying Braak stage I pathology shows significantly higher levels of granular tau oligomer formation than that displaying Braak stage 0 pathology (22), indicating that before NFTs form, tau initiates the formation of different types of aggregates that may play a role in neuronal death and neuronal dysfunction.

In the present study, to understand the role of tau aggregation in neuronal death and neuronal dysfunction, we assessed and compared neuronal death, NFT formation, tau phosphorylation state, synapse number, and behavior in mice that express P301L mutant tau and compared these with mice that express human wild-type tau. The same type of promoter was used to drive tau expression in both lines of mice.

EXPERIMENTAL PROCEDURES

Animals—Generation of Tg mouse lines expressing P301L mutant human tau was performed as described (23). A cDNA construct of P301L mutant human tau was inserted into a CaM kinase II chain expression vector at XhoI sites. A 4.3-kb BglII-NaeI fragment containing the CaM kinase II promoter-P301L mutant human tau cDNA and a 3′-untranslated se-

* This work supported in part by a grant-in-aid for Scientific Research on Priority Areas (Research on Pathomechanisms on Brain Disorders) from the Ministry of Education, Culture, Sports, Science, and Technology of Japan.

[S] The on-line version of this article (available at http://www.jbc.org) contains supplemental Fig. 1.

[1] To whom correspondence should be addressed. Tel.: 81-48-467-9627; Fax: 81-48-467-5916; Email: kenneth@brain.riken.jp.

[2] The abbreviations used are: NFT, neurofibrillary tangles; FTDP-17, frontotemporal dementia with parkinsonism linked to chromosome 17; CaM, calmodulin; TA, temporal area; BLA, basolateral amygdala; LA, lateral amygdala; EC, entorhinal cortex; Tg, transgenic.

quence were used as the transgenes to create the P301Ltau-Tg mice on a C57BL/6J background.

Antibodies—For immunohistochemistry and immunoblotting, we used the following antibodies: rabbit polyclonal anti-tau JM; phosphorylation-independent monoclonal anti-tau TauN; phosphorylation-dependent mouse monoclonal anti-tau AT180 (Innogenetics Zwijndrecht, Belgium), which recognizes tau phosphorylated at Thr-231; AT8 (Innogenetics Zwijndrecht), which recognizes tau phosphorylated at Ser-199, Ser-202, and Thr-205; PHF1 (generously provided by Dr. Peter Davies, Albert Einstein College of Medicine, NY), which recognizes tau phosphorylated at Ser-396 and Ser-404; dephosphorylation-dependent mouse monoclonal anti-tau Tau1, which recognizes tau-dephosphorylated Ser-199 and Ser-202; phosphorylation-dependent rabbit polyclonal anti-tau Thr(P)-205, Thr(P)-212, Ser(P)-396, Ser(P)-400, Ser(P)-404, and Ser(P)-422, which recognize tau phosphorylated at Thr-205, Thr-212, Ser-396, Ser-400, Ser-404, and Ser-422, respectively.

Western Blotting—Mouse brains were homogenized in Tris-buffered saline (TBS; 10 mM Tris, 150 mM NaCl, pH 7.4) containing protease inhibitors (1 μg/ml antipine, 5 μg/ml pepstatin, 5 μg/ml leupeptin, 2 μg/ml aprotinin, 0.5 μM 4-(2-aminoethyl)benzenesulfonyl fluoride hydrochloride), and phosphatase inhibitors (1 mM NaF, 0.4 mM Na_3VO_4, and 0.5 mM okadaic acid). After centrifugation at 100,000 $\times$ *g* for 20 min, the supernatant was collected. Sarcosyl-insoluble, paired helical filament-enriched fractions were prepared from TBS-insoluble pellets according to the procedure developed by Greenberg and Davies (24). The resulting precipitate was rehomogenized in 5 volumes of 0.8 M NaCl and 10% sucrose solution and centrifuged at 100,000 $\times$ *g* for 20 min. A one-tenth volume of 10% sarcosyl solution was added to the supernatant, which was then mixed by vortex, incubated for 1 h at 37 °C, and centrifuged at 150,000 $\times$ *g* for 1 h. The resulting pellet was analyzed as the sarcosyl-insoluble fraction. TBS-soluble and sarcosyl-insoluble materials were solubilized in Laemmli sample buffer and subjected to SDS-PAGE. Separated proteins were blotted onto Immobilon-P membranes (Millipore). The membranes were incubated with primary antibody followed by the appropriate-species HRP-conjugated secondary antibody. Chemiluminescent detection (ECL, Amersham Biosciences) was used for visualization. Quantitation and visual analysis of immunoreactivity were performed with a computer-linked LAS-3000 Bio-Imaging Analyzer System (Fujifilm).

Histology and Immunohistochemical Procedures—Mice were deeply anesthetized with pentobarbital (50 mg/kg), then transcardially perfused with 10% formalin. Brains were post-fixed in the same fixative for 16 h and embedded in paraffin and sectioned (4–6 μm) in the coronal plane. Deparaffinized sections were treated with Target Retrieval Solution (Dako) for 20 min at 80 °C, blocked in 0.1% BSA/TBS, and incubated with primary antibodies in 0.1% BSA/TBS overnight at 4 °C. A fluorescent microscope equipped with a cooled CCD camera and Neurolucida software (Version 7; MicroBrightField Inc., Williston, VT) were used to analyze the sections and for acquisition of images under virtual slice mode. NFTs were identified by means of the standard Gallyas silver-impregnation method (10).

For immunostaining of PSD95, deparaffinized coronal sections were treated with proteinase K solution (100 μM in PBS) for 10 min at 37 °C and incubated with anti-PSD95 antibody. PSD95 immunoreactivity in layer I of the left and right visual cortex and layer I of lateral entorhinal cortex (4.2–4.5 mm posterior to bregma) were quantitated with a fluorescence microscope equipped with a cooled CCD camera and Neurolucida software (Version 7; MicroBrightField Inc., Williston, VT). Quantitative results were presented as normalized intensity values that were determined by dividing fluorescence intensity of entorhinal layer I by that of ipsilateral visual cortex.

Stereological Analysis—We estimated neuronal density in the temporal neocortex (TA), lateral entorhinal cortex (EC), lateral amygdala (LA), and basolateral amygdala (BLA) by counting neurons in each area of serial coronal brain sections obtained from three Wtau-Tg mice (male, 23 months old) and three P301Ltau-Tg mice (male, 22 months old). Each section was stained with cresyl violet and examined with a microscope linked to a Neurolucida tracing system. In the present study, due to variations in the structural complexity of the regions of interest, the strategy we selected for estimating neuronal density was to measure the mean number of neurons located within 100-μm^2 counting boxes covering all neurons within each region of interest. Each region of interest was selected and delineated by an expert in mouse brain cytoarchitectonics (Dr. T. Fukuda), and neuronal counting was performed using the Neurolucida system by researchers who were blind to identifying information about the sections (*e.g.* source animals, age of animals, etc.). For the amygdala, we analyzed sections that were about 50 μm apart, and for the cortices, we analyzed sections that were 300 μm apart (three sections containing each region from each animal were analyzed).

Morris Water Maze Test—To assess place learning and memory performance of P301Ltau-Tg mice, we used a cylindrical test apparatus (1 m in diameter) and task-fashioned after the Morris water maze. The water was maintained at 24 °C, and the maze was surrounded by landmark objects placed in the room. A slightly submerged transparent platform to which the mice could escape was hidden from view by making the water opaque with a white bio-safe material. The position of the platform was fixed during a 60-s test period.

Mouse behavior and swimming paths during the water maze test were monitored and recorded by a CCD camera mounted overhead; digital data of real-time images were recorded to a PC using the public domain NIH Image program (developed at The United States National Institutes of Health and available on the Internet at rsb.info.nih.gov/nih). Images of the mouse were sampled at 2 Hz. Data were analyzed using customized software based on Matlab (Version 7.2, Mathworks Co. Ltd., Natick, MA) with image analysis tool box (Mathworks Co. Ltd.). During testing, the sequential position of the mouse was determined in each video frame, and the swimming speed, distance from the platform, and latency to reach the platform were calculated. To assess learning, we measured the distance between the mouse and the platform

every 0.5 s until the mouse reached the platform. Next, we calculated the total distance traveled by the mouse by integrating the distance between the mouse and the platform. This "integral distance" value represents the error score. We used this error score as a measure of learning performance.

For learning trials, the mouse was gently placed on the water surface close to the cylinder wall in the opposite half of the maze away from the platform; it was allowed to swim freely for a 60-s test period. When the mouse did not escape to the submerged platform within this test period, we gently navigated it to the platform by hand and made it stay there for 20 s. For each mouse, we carried out three learning trials per day for nine successive days. A single probe test was given on the 10th day in which the platform was removed from the maze in the absence of the mouse . The mouse was introduced into the maze as before and allowed to search for the missing platform for 60 s.

An error score for the probe test was calculated by measuring the total distance the mouse traveled for 60 s. Statistical analyses were conducted using PRISM4 (GraphPad Software Inc., La Jolla CA). Data were analyzed using the Friedman test or two-way analysis of variance unless noted otherwise. If a mouse remembered the location of the platform during training, its probe score (error score per frame) was small, because the mouse spent most of its time searching the area where the platform was formerly located.

RESULTS

Expression of P301L Mutant Tau in Mouse Brain—CaM kinase II promoter regulated the expression of P301L mutant human 4 repeat tau in P301Ltau-Tg mice (Fig. 1*A*); CaM kinase II promoter also regulated the expression of wild-type tau in Wtau-Tg mice. The pattern of tau expression in different brain regions was determined by immunoblotting using TauN antibody (Fig. 1*B*), which recognizes the N terminus of tau. Cerebral cortex, hippocampus, and striatum showed the highest levels of P301L mutant human 4 repeat tau expression, 3–5-fold greater than that of endogenous tau. Thalamus, olfactory bulb, and midbrain had moderate levels, whereas in medulla, cerebellum, and spinal cord, expression of P301L mutant human 4 repeat tau was not detected. There were no differences in the expression patterns between male and female mice or between young and old mice. Wild-type and mutant human tau expression patterns in P301Ltau-Tg and Wtau-Tg mice were the same; however, P301Ltau-Tg mice had about 1.8-fold more human tau in cerebral cortex, hippocampus, entorhinal cortex, and striatum than Wtau-Tg mice.

Less Phosphorylation and Greater Insolubility of P301L Tau—To assess tau phosphorylation state and aggregation, we prepared P301Ltau-Tg mouse brain (hippocampus) homogenates in TBS and analyzed tau in the soluble fraction. We previously observed that Wtau-Tg mice show age-dependent increases in tau phosphorylation (23); thus, in the present study, we compared the tau phosphorylation state in old P301Ltau-Tg mice and old Wtau-Tg mice (Fig. 2*A*). Although the phosphorylation-independent tau antibody TauN prominently labeled the faster mobility human tau band derived

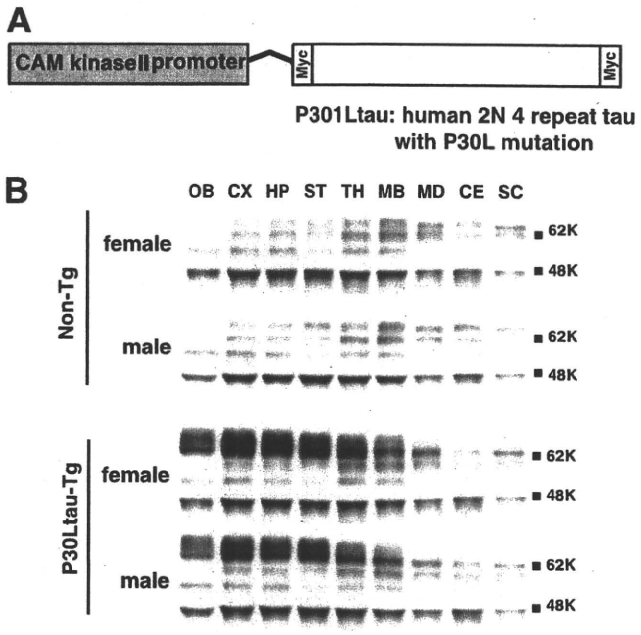

FIGURE 1. **Generation of a transgenic mouse expressing P301L mutant human 2N/4 repeat tau.** *A*, a diagram shows that the expression of mutant P301L human 4 repeat tau tagged with myc and FLAG epitopes was regulated by the CaM kinase II promoter. *B*, Western blots show the pattern of tau expression in different brain regions. Blots were probed with anti-tauN antibody, which recognizes the N terminus of tau. Male and female mice did not exhibit different expression patterns. *OB*, olfactory bulb; *CE*, cerebellum; *CX*, cerebral cortex; *HP*, hippocampus; *MB*, midbrain; *SC*, spinal cord; *ST*, striatum; *TH*, thalamus; *MD*, medulla.

from P301Ltau-Tg samples (*filled arrowheads*), it also labeled the slower mobility human tau band derived from Wtau-Tg samples (*open arrowheads*), suggesting that P301L mutant tau in the brains of aged mice may be less phosphorylated than wild-type human tau.

Next, we analyzed the phosphorylation state of individual sites on tau using different phosphorylation-dependent tau antibodies. Tau1, a dephosphorylation-dependent anti-tau antibody, primarily labeled the faster mobility human tau band from Wtau-Tg and P301Ltau-Tg samples. However, normalized tau immunoreactivity (normalized to TauN immunoreactivity) was significantly greater in samples derived from P301Ltau-Tg mice than in those from Wtau-Tg mice. AT8, which recognizes tau phosphorylated at Ser-199, Ser-202, and Thr-205, anti-Thr(P)-205 antibody, which recognizes tau phosphorylated at Thr-205, and anti-Thr(P)-212 antibody, which recognizes tau phosphorylated at Thr-212, labeled the slower mobility human tau band from Wtau-Tg and P301Ltau-Tg samples. Band intensities were normalized by the intensity of the TauN band (Fig. 2*A*, *left panel*). Normalized immunoreactivities of Thr(P)-205- and Thr(P)-212-immunoreactive human tau bands were significantly lower in P301Ltau-Tg than in Wtau-Tg samples. AT8 also showed the same tendency, although it was not statistically significant at $p < 0.05$. AT180, which recognizes tau phosphorylated at Thr-231, primarily labeled the slower mobility human tau band from both Tg mouse line samples; there was no difference in the normalized AT180 immunoreactivity between samples from Wtau-Tg and P301Ltau-Tg mice. Ser(P)-396,

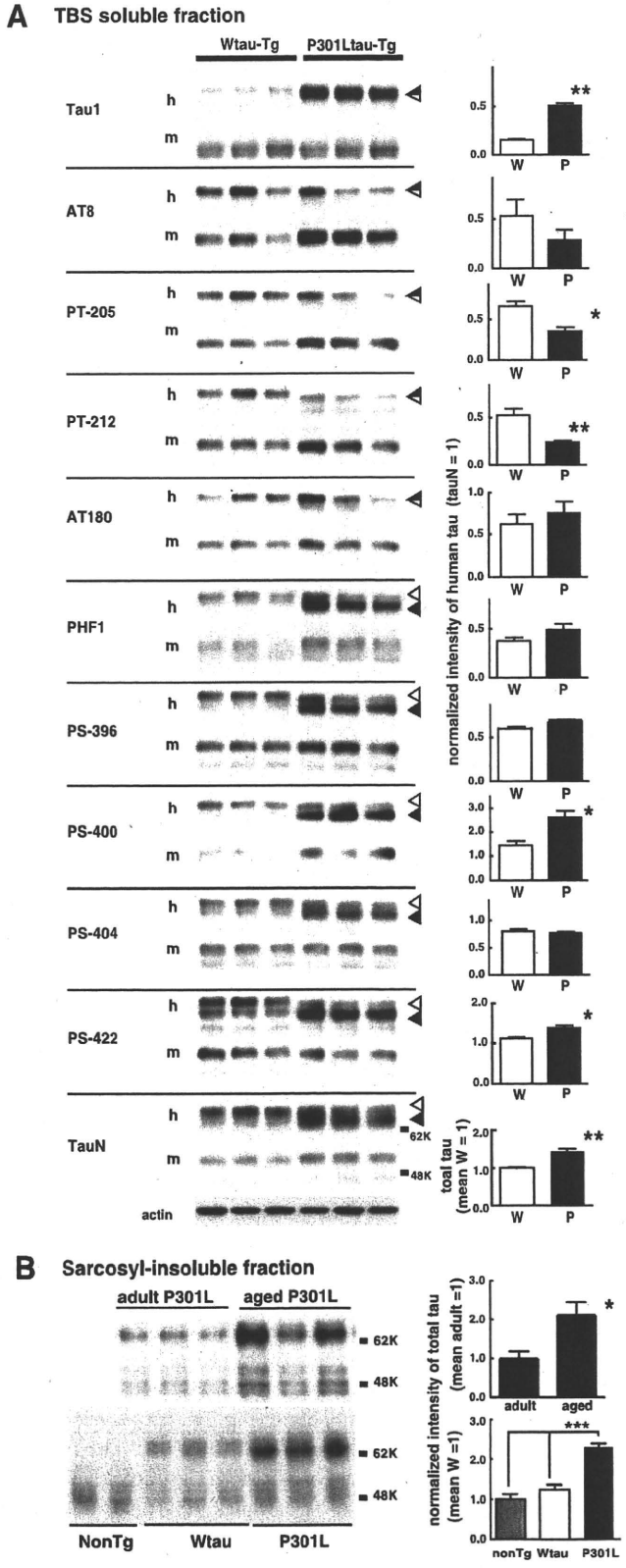

FIGURE 2. **The brains of P301L-Tg mice form sarcosyl-insoluble tau aggregates, but tau from P301L-Tg mice is less phosphorylated than that from Wtau-Tg mice.** *A*, Western blots of TBS-soluble fractions from the brain homogenates of 22-month-old P301Ltau-Tg mice and 22-month-old Wtau-Tg mice (*left panel*) and histograms show the corresponding tau intensity levels normalized according to TauN immunoreactivity (*right panel*; *W*, Wtau-Tg mice; *P*, P301Ltau-Tg mice). The immunoblots were probed with various anti-tau antibodies, as indicated. Anti-Thr(P)-205, anti-Thr(P)-212, anti-Ser(P)-396, anti-Ser(P)-400, and anti-Ser(P)-422 recognize tau phosphorylated at Thr-205, Thr-212, Ser-396, Ser-400, Ser-404, and Ser-422, respectively. TauN recognizes total phosphorylation-independent tau; AT8 recognizes tau phosphorylated at Ser-199, Ser-202, and Thr-205; AT180 recognizes tau phosphorylated at Thr-231; PHF1 recognizes tau phosphorylated at Ser-396 and Ser-404; actin is shown as an internal control. *Open arrowheads* indicate the mobility of wild-type human tau bands; *filled arrowheads* indicate the mobility of the P301L human tau bands. Data are represented as the averages ± S.E. *, $p < 0.05$ (Mann-Whitney test); **, $p < 0.01$ (Mann-Whitney test). *B*, *upper left panel*, Western blots of sarcosyl-insoluble fractions from the brain homogenates of 10-month-old P301Ltau-Tg mice (adult) and 22-month-old P301Ltau-Tg mice (aged) are shown. Immunoreactivities were quantified and represented as averages ± S.E. ($n = 5$). *, $p < 0.05$ (Mann-Whitney test) (*upper right panel*), *Lower panel*, Western blots are shown of sarcosyl-insoluble fractions from the brain homogenates of aged (22–24 months old) non-Tg, Wtau-Tg, and P301Ltau-Tg mice. Immunoreactivities were quantified and are represented as averages ± S.E. ($n = 5$). *, $p < 0.05$; ***, $p < 0.005$ (Mann-Whitney test) (*lower right panel*). Immunoreactivities of sarcosyl-insoluble tau in Wtau-Tg mice were similar to levels in non-Tg mice.

which recognizes tau phosphorylated at Ser-396, and Ser(P)-404, which recognizes tau phosphorylated at Ser-404, primarily labeled the faster mobility human tau band derived from P301Ltau-Tg samples but primarily labeled the slower human tau band derived from Wtau-Tg samples. Normalized immunoreactivities of Ser(P)-396 and Ser(P)-404 did not significantly differ between P301Ltau-Tg and Wtau-Tg mice; PHF1 immunoreactivity also did not differ between P301Ltau-Tg and Wtau-Tg mice. Anti-Ser(P)-400, which recognizes tau phosphorylated at Ser-404, and anti-Ser(P)-422, which recognizes tau phosphorylated at Ser-422, primarily labeled the faster mobility human tau band derived from P301Ltau-Tg samples but primarily labeled the slower human tau band derived from Wtau-Tg samples. Normalized immunoreactivities for both antibodies were significantly greater in P301Ltau-Tg than in Wtau-Tg mice.

In general, P301L mutant human tau tended to be less phosphorylated in its N terminus projection region but more phosphorylated in its C terminus compared with wild-type human tau. All phosphorylation-dependent antibodies recognized the slower mobility band from Wtau-Tg samples. With respect to P301Ltau-Tg samples, however, phosphorylation-dependent antibodies recognizing the C terminus region labeled the faster mobility tau band, whereas phosphorylation-dependent antibodies recognizing the N terminus projection region labeled the slower mobility tau band. These results suggest that the brains of aged P301Ltau-Tg mice have lower levels of fully phosphorylated tau than the brains of aged Wtau-Tg mice.

In addition to analyzing the P301L tau phosphorylation state in mouse brain, we investigated the solubility of P301L tau in sarcosyl solution (Fig. 2). As previously mentioned, we did not recover human tau in sarcosyl-insoluble fractions derived from the brains of Wtau-Tg mice (10) (Fig. 2*B*, *lower panel*). In the present study, however, we recovered more human tau in the sarcosyl-insoluble fraction derived from the brains of aged P301Ltau-Tg mice with age-dependent manner (Fig. 2*B*, *upper panel*). We also confirmed that P301Ltau-Tg mice have lower levels of fully phosphorylated tau than Wtau-Tg mice. Taken together, these results indicate that,

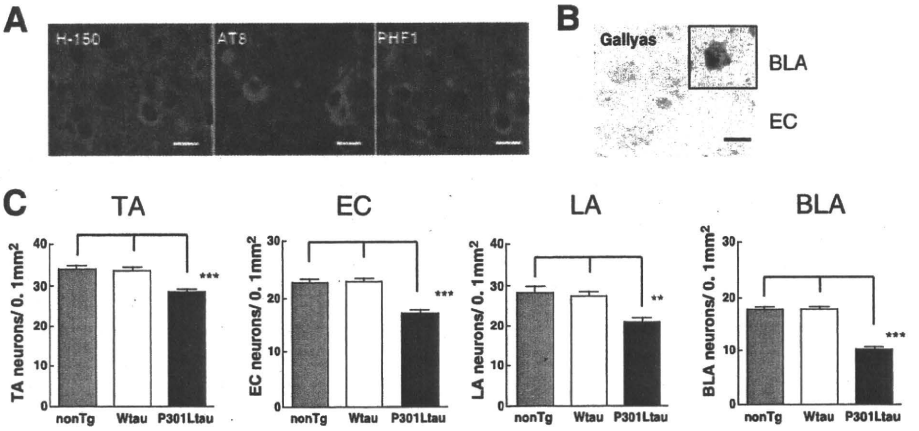

FIGURE 3. **The brains of P301Ltau-Tg mice display neuron loss but not NFTs.** *A*, entorhinal cortex sections immunostained with phosphorylation-independent anti-human tau antibody (H-150) or phosphorylation-dependent anti-tau antibodies (AT8 and PHF1) are shown. Phosphorylated human tau accumulated in cell bodies and dendrites of neurons in the entorhinal cortex. *B*, shown is the entorhinal cortex section stained with the Gallyas silver staining method. No silver-stained neurons were seen in the entorhinal cortex, but silver-stained neurons were occasionally seen in the BLA. *C*, histograms show the numbers of neurons counted in the TA of neocortex (*NC*), EC, LA, and BLA of Non-Tg, Wtau-Tg, and P301Ltau-Tg mice. Three cresyl violet-stained brain sections containing each region were analyzed, and the number of neurons in each region was counted using a Neurolucida system ($n = 3$ mice for each group). For the amygdala, we analyzed sections that were about 50 μm apart, and for neocortex and entorhinal cortex, we analyzed sections that were 300-μm apart. Data are represented as the averages ± S.E. *, $p < 0.05$ (Mann-Whitney test); **, $p < 0.01$ (Mann-Whitney test); ***, $p < 0.005$ (Mann-Whitney test). *A* and *B scale bars*, 10 μm.

although less phosphorylated than wild-type tau, P301L mutant tau could form sarcosyl-insoluble tau aggregates. In other words, P301L tau can form tau aggregates in even less tau phosphorylation states compare with Wtau-Tg mouse.

P301L tau-Tg Mice Exhibit Neuron Loss but Not NFTs—To understand how tau aggregation affects NFT formation and neuron loss, we examined P301Ltau-Tg mouse brains using immunohistochemical and silver-staining methods (Fig. 3). Some neurons were immunoreactive for phosphorylation-dependent anti-tau antibodies (Fig. 3*A*). Phosphorylated tau accumulated in cell bodies and dendrites of neurons. Most neurons, however, were negative for Gallyas silver staining (Fig. 3*B*). Only occasional Gallyas-positive neurons were observed in lateral amygdala (Fig. 3*B*, *inset*). Therefore, although phosphorylated tau accumulated in some neurons, NFTs did not form in most neurons.

Next, we assessed the number of neurons in the TA, EC, LA, and BLA of non-Tg, Wtau-Tg, and P301Ltau-Tg mice (Fig. 3*C*). The density of neurons in TA, EC, LA, and BLA of P301Ltau-Tg mice was significantly reduced compared with that of non-Tg and Wtau-Tg mice (Fig. 3*C*). Neuron counts in these areas of Wtau-Tg and non-Tg mice were not significantly different, as previously reported (23) (Fig. 3*C*). P301Ltau-Tg mice had neuron loss in various brain regions that also exhibited sarcosyl-insoluble tau aggregation but no NFTs. These results suggest that an accumulation of sarcosyl-insoluble tau aggregates in the brains of P301Ltau-Tg mice may be involved in neuronal loss, as Wtau-Tg mice displayed neither sarcosyl-insoluble tau nor neuron loss.

P301L Tau-Tg Mice Lack Behavioral Signs of Brain Dysfunction—The EC is an important brain region involved in memory. Because P301Ltau-Tg mice exhibited significant neuron loss in the EC, we tested P301Ltau-Tg mice in the Morris Water Maze, a behavioral task that assesses place learning and memory. As shown in Fig. 4*A*, the mean error scores of P301Ltau-Tg mice diminished with repetitive training, as did those of non-Tg mice. Consistent with our previous findings, the mean error scores of Wtau-Tg mice did not, however, decrease (23). In the probe test, P301Ltau-Tg and non-Tg mice remembered the maze quadrant in which the escape platform was located and had significantly lower probe scores than Wtau-Tg mice (Fig. 4*B*). This suggests that the neuron loss in P301Ltau-Tg mice did not affect their ability to form memories.

In a previous report we demonstrated that the EC of Wtau-Tg mice have fewer synapses than non-Tg mice and that this decrease in synapses was associated with memory impairment (23). To determine whether P301Ltau-Tg mice have fewer synapses, we compared immunoreactivity for PSD95, a postsynaptic marker, in brain sections from P301Ltau-Tg, Wtau-Tg, and non-Tg mice (Fig. 4*C*). PSD95 immunoreactivity in the visual cortex (V2) did not differ in non-Tg, Wtau-Tg, and P301Ltau-Tg mice (Fig. 4*C*). PSD95 immunoreactivity in the EC of non-Tg and P301Ltau-Tg mice did not differ significantly (Fig. 4, *C* and *D*). However, PSD95 immunoreactivity in the EC of Wtau-Tg mice was significantly reduced (Fig. 4, *C* and *D*), which was confirmed by synaptophysine immunoreactivity in P301Ltau-Tg, Wtau-Tg, and non-Tg mice (**supplemental Fig. 1**). These results indicate that the sarcosyl-insoluble tau of P301Ltau-Tg mice may be involved in neuron loss but not in synapse loss. This may explain why P301Ltau-Tg mice retain the ability to form place memories despite exhibiting significant neuronal loss.

DISCUSSION

P301L Tau Mutation—The P301L human tau-overexpressing mouse was generated and showed NFTs and neuronal loss (3, 4). Lines of rTg4510 mice (14) show a 7-fold overexpression of P301L tau relative to endogenous mouse tau and start to display pretangles at 14.5 months of age. By contrast, another line of mice that shows a 13-fold overexpression of P301L tau begins to exhibit argyrophilic NFT-like pathology

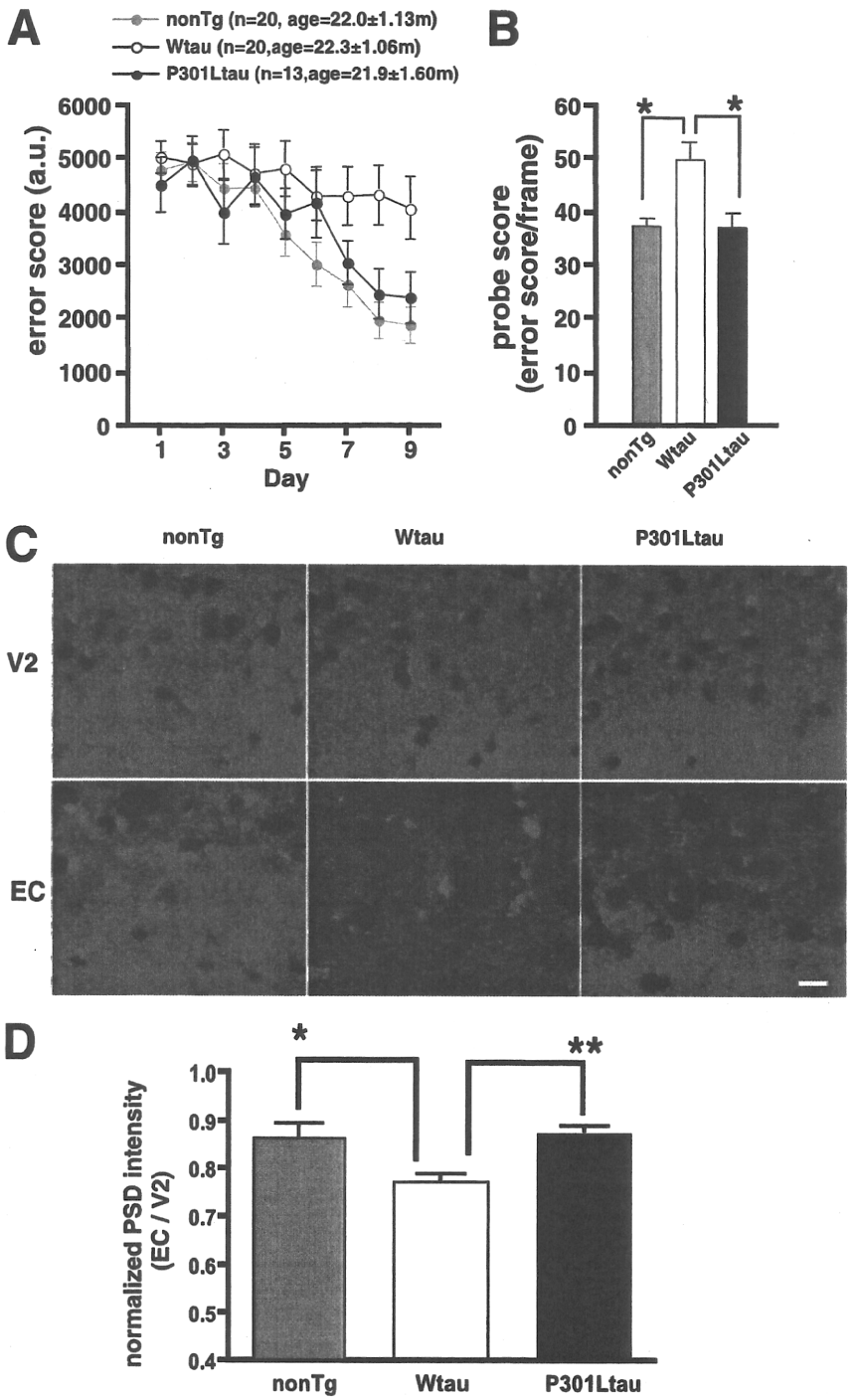

FIGURE 4. **Aged P301Ltau-Tg mice have normal place learning and memory.** The Morris water maze was used to assess the place learning and memory of aged (20–24 months old) non-Tg ($n = 20$), Wtau-Tg ($n = 20$), and P301Ltau-Tg ($n = 13$) mice. *A*, learning and memory performance are expressed as error scores. Learning curves and memory performance of non-Tg and P301Ltau-Tg mice were not significantly different ($p < 0.577$, $F = 0.449$, repeated measures two-way analysis of variance). However, Wtau-Tg mice took significantly longer than non-Tg mice to learn the task ($p < 0.0326$, $F = 4.92$, repeated measures two-way analysis of variance). *a.u.*, arbitrary units. *B*, probe scores of P301Ltau-Tg and non-Tg mice were not different ($p > 0.05$, Dunn's multiple comparison test). However, the probe scores of Wtau-Tg mice were worse than those of non-Tg mice and P301Ltau-Tg mice ($p < 0.05$ for each, Dunn's multiple comparison test). Probe score is a measure of memory performance. *C*, shown are coronal brain sections from non-Tg, Wtau-Tg, and P301Ltau-Tg mice. The sections were immunostained with anti-PSD95 antibody, an antibody against the post-synaptic marker PSD95. Consistent with the learning and memory performance results, PSD95 immunoreactivity in the entorhinal cortex of non-Tg and P301Ltau-Tg mice were not different. However, PSD95 immunoreactivity was reduced in the entorhinal cortex of Wtau-Tg mice. *D*, shown is quantitative analysis of PSD95 immunoreactivity in entorhinal cortex. Results are expressed as fluorescence intensity of layer I of the lateral entorhinal cortex normalized by that of layer I of ipsilateral visual cortex (non-Tg, $n = 7$; Wtau-Tg, $n = 6$; and P301L-Tg, $n = 3$). Measurements were done on coronal brain sections. Dunn's multiple comparison test revealed a significant difference in PSD95 immunoreactivity between Wtau-Tg and P301L-Tg mice ($p < 0.01$). Data are represented as averages ± S.E. *, $p < 0.05$; **, $p < 0.01$. *V2*, visual cortex.

at 5.5 months of age (13). Moreover, the amount of sarcosyl-insoluble tau and the number of NFTs in these mice is correlated. In the present study our P301Ltau-Tg mice showed a 3–5-fold overexpression of P301L tau relative to endogenous mouse tau and formed sarcosyl-insoluble tau with few argyrophilic NFTs at 22 months of age. The differences displayed by these three lines of mice may be due to the varying degrees of P301L tau expression in these mice. On the other hand, our Wtau-Tg mice, expressing 2–3-fold wild human tau relative to endogenous mouse tau, did not form sarcosyl insoluble tau, and the other mouse lines overexpressing 4–15-fold wild human tau relative to endogenous mouse tau have not reported the formation of sarcosyl insoluble tau aggregation (25). The difference between our Wtau- and P301Ltau-Tg shown here may be due not to tau expression levels but to the existence of FTDP-17 mutation.

Tau Phosphorylation and Aggregation—The present analysis of P301Ltau-Tg mice suggests that tau with the P301L mutation forms sarcosyl-insoluble tau even though it is less phosphorylated than wild-type tau. These findings are supported by the *in vitro* observations that P301L tau only requires 4–6 mol of phosphate per tau to polymerize into filaments, whereas wild-type tau requires more than 10 mol of phosphate per tau for self-aggregation (26). This is likely due to the fact that tau with the FTDP-17 mutation enhances the formation of local β-structures (27), which may promote tau aggregation faster than what occurs with wild-type tau. Thus, before becoming hyperphosphorylated, P301L mutant tau can begin to self-aggregate. We also found that P301Ltau was less phosphorylated in mouse brain than wild-type human tau. Phosphorylation state, however, can affect tau conformation. Jeganathan *et al.* (28) reported that tau in solution adopts a "paperclip" conformation. Pseudophosphorylation of either the AT8 site or the PHF1 site causes the paperclip conformation to open up, whereas pseudophosphorylation of both AT8 and PHF1 sites causes tau to form a compact paperclip conformation (28). Additional phosphorylation induces pathological conformational changes (28).

When AT8 sites are pseudo-phosphorylated, the distance between the tau N and C termini is longer than when PHF1 sites or AT8 and PHF1 sites are pseudo-phosphorylated (28). For the latter situations, the distances between the tau C and N termini are similar. In the present study we found that the PHF1 site of P301L tau was phosphorylated to a similar extent as wild-type tau, whereas the AT8 site of P301L tau was phosphorylated to a lesser extent than wild-type tau. This may be because P301L tau could form aggregates before phosphorylation of tau at N-terminal site. Nonetheless, P301L tau formed sarcosyl-insoluble tau aggregates even though it was not fully phosphorylated. If shortening the distance between the C and N termini of tau is the minimum requirement needed for tau to adopt a pathological conformation, phosphorylation of the C-terminal region of P301L tau may be sufficient for it to form a pathological conformation, resulting in the formation of sarcosyl-insoluble tau aggregates. Although aged Wtau-Tg mice formed hyperphosphorylated tau, they did not form insoluble tau aggregates. This may be because hyperphosphorylated tau levels in these mice are lower than those needed for inducing the formation of insoluble tau.

Tau Aggregation Induces Neuron Loss and NFT Formation—Although P301Ltau-Tg mice formed sarcosyl-insoluble tau that was accompanied by neuron loss, they did not form Gallyas silver-impregnated NFTs, suggesting that NFT formation and neuron loss might occur through different tau-related mechanisms. This notion is supported by a previous report (14). Thus, an aggregated form of tau included in sarcosyl-insoluble fraction might contribute to neuronal loss. In an *in vitro* tau aggregation system, we have found that the sarcosyl-insoluble fraction contains granular tau oligomers and tau fibrils (22). Because NFTs consist of bundles of tau fibrils, the observation that P301L tau formed sarcosyl-insoluble aggregates in brains without forming NFTs suggests that the neurons of P301Ltau-Tg mice produce large amounts of granular tau oligomers but few fibrils. If this is indeed the case, granular tau oligomer can be considered to be a toxic tau aggregate species.

Shiarli *et al.* (29) compared the differences between FTDP-17 and AD and found that, whereas the tissue loss is greater in FTPD-17, the amount of NFTs is about one-tenth that in AD. This observation suggests that FTDP-17-related mutant tau tends to induce neuronal loss rather than the formation of NFTs. As with FTDP-17 patients, our P301L tau mice tend to display more neuronal loss than NFT formation.

Tau-induced Synapse Loss and Neuron Loss—Wtau-Tg mice exhibit memory impairment in the absence of sarcosyl-insoluble tau aggregate formation (23). By contrast, P301Ltau-Tg mice did not exhibit memory impairment even though they exhibited neuron loss and formed sarcosyl-insoluble tau aggregates. The memory impairment disparity between Wtau-Tg and P301Ltau-Tg mice may due to decreased PSD95 immunoreactivity and, hence, fewer synapses in the EC of Wtau-Tg mice (23). The present study demonstrated that PSD95 immunoreactivity in the EC of P301Ltau-Tg mice was comparable with that of Non-Tg mice even though the number of EC neurons in P301Ltau-Tg mice was about 77% that in non-Tg mice. That the number of synapses in P301Ltau-Tg mice was not reduced suggests the remaining neurons sufficiently maintain neuronal function by increasing the number of synapses (30, 31). The observation that P301Ltau-Tg mice display enhanced long term potentiation (32) before NFT formation supports the premise that an increase in the number of synapses may compensate for the reduction in the number of neurons. Indeed, a more than 50% neuron loss in hippocampus could not compensate for neuronal function, as such a loss was found to impair memory formation (14).

In P301Ltau-Tg mice, neuron loss occurred without affecting the number of synapses, whereas in Wtau-Tg mice synapse loss occurred without affecting the number of neurons. Moreover, P301Ltau-Tg mice formed less phosphorylated forms of tau and formed sarcosyl-insoluble tau aggregates, whereas Wtau-Tg mice formed hyperphosphorylated tau but did not form sarcosyl-insoluble tau aggregates. Therefore, the soluble form of hyperphosphorylated tau may be involved in synapse loss, whereas the insoluble form of tau may be in-

volved in neuron loss. During neurodegeneration, tau becomes hyperphosphorylated and forms a very compact paperclip-like structure (33), one that induces synaptic loss. Concurrently, increasing concentrations of hyperphosphorylated tau induce the formation of granular tau oligomers, which are not synaptotoxic but do cause neuronal loss. As the concentration of granular tau oligomers increases, a non-neurotoxic form of tau (fibrillar tau) forms, ultimately leading to the formation of NFTs. Different forms of tau aggregates may be involved in the different pathological features of neurodegeneration.

REFERENCES

1. Gómez-Isla, T., Hollister, R., West, H., Mui, S., Growdon, J. H., Petersen, R. C., Parisi, J. E., and Hyman, B. T. (1997) *Ann. Neurol.* **41,** 17–24
2. Ingelsson, M., Fukumoto, H., Newell, K. L., Growdon, J. H., Hedley-Whyte, E. T., Frosch, M. P., Albert, M. S., Hyman, B. T., and Irizarry, M. C. (2004) *Neurology* **62,** 925–931
3. Goedert, M., and Spillantini, M. G. (2000) *Biochim. Biophys. Acta* **1502,** 110–121
4. Hutton, M. (2000) *Ann. N.Y. Acad. Sci.* **920,** 63–73
5. Dawson, H. N., Cantillana, V., Chen, L., and Vitek, M. P. (2007) *J. Neurosci.* **27,** 9155–9168
6. Goedert, M., and Jakes, R. (2005) *Biochim. Biophys. Acta* **1739,** 240–250
7. Götz, J., Streffer, J. R., David, D., Schild, A., Hoerndli, F., Pennanen, L., Kurosinski, P., and Chen, F. (2004) *Mol. Psychiatry* **9,** 664–683
8. Lewis, J., McGowan, E., Rockwood, J., Melrose, H., Nacharaju, P., Van Slegtenhorst, M., Gwinn-Hardy, K., Paul Murphy, M., Baker, M., Yu, X., Duff, K., Hardy, J., Corral, A., Lin, W. L., Yen, S. H., Dickson, D. W., Davies, P., and Hutton, M. (2000) *Nat. Genet.* **25,** 402–405
9. Pérez, M., Ribe, E., Rubio, A., Lim, F., Morán, M. A., Ramos, P. G., Ferrer, I., Isla, M. T., and Avila, J. (2005) *Neuroscience* **130,** 339–347
10. Tanemura, K., Akagi, T., Murayama, M., Kikuchi, N., Murayama, O., Hashikawa, T., Yoshiike, Y., Park, J. M., Matsuda, K., Nakao, S., Sun, X., Sato, S., Yamaguchi, H., and Takashima, A. (2001) *Neurobiol. Dis.* **8,** 1036–1045
11. Taniguchi, T., Doe, N., Matsuyama, S., Kitamura, Y., Mori, H., Saito, N., and Tanaka, C. (2005) *FEBS Lett.* **579,** 5704–5712
12. Sato, S., Tatebayashi, Y., Akagi, T., Chui, D. H., Murayama, M., Miyasaka, T., Planel, E., Tanemura, K., Sun, X., Hashikawa, T., Yoshioka, K., Ishiguro, K., and Takashima, A. (2002) *J. Biol. Chem.* **277,** 42060–42065
13. Ramsden, M., Kotilinek, L., Forster, C., Paulson, J., McGowan, E., SantaCruz, K., Guimaraes, A., Yue, M., Lewis, J., Carlson, G., Hutton, M., and Ashe, K. H. (2005) *J. Neurosci.* **25,** 10637–10647
14. Santacruz, K., Lewis, J., Spires, T., Paulson, J., Kotilinek, L., Ingelsson, M., Guimaraes, A., DeTure, M., Ramsden, M., McGowan, E., Forster, C., Yue, M., Orne, J., Janus, C., Mariash, A., Kuskowski, M., Hyman, B., Hutton, M., and Ashe, K. H. (2005) *Science* **309,** 476–481
15. Spires, T. L., Orne, J. D., SantaCruz, K., Pitstick, R., Carlson, G. A., Ashe, K. H., and Hyman, B. T. (2006) *Am. J. Pathol.* **168,** 1598–1607
16. Barghorn, S., Zheng-Fischhöfer, Q., Ackmann, M., Biernat, J., von Bergen, M., Mandelkow, E. M., and Mandelkow, E. (2000) *Biochemistry* **39,** 11714–11721
17. Lee, S., Jung, C., Lee, G., and Hall, G. F. (2009) *J. Alzheimers Dis.* **16,** 99–111
18. Nacharaju, P., Lewis, J., Easson, C., Yen, S., Hackett, J., Hutton, M., and Yen, S. H. (1999) *FEBS Lett.* **447,** 195–199
19. Miyasaka, T., Morishima-Kawashima, M., Ravid, R., Heutink, P., van Swieten, J. C., Nagashima, K., and Ihara, Y. (2001) *Am. J. Pathol.* **158,** 373–379
20. Maeda, S., Sahara, N., Saito, Y., Murayama, M., Yoshiike, Y., Kim, H., Miyasaka, T., Murayama, S., Ikai, A., and Takashima, A. (2007) *Biochemistry* **46,** 3856–3861
21. Kimura, T., Yamashita, S., Nakao, S., Park, J. M., Murayama, M., Mizoroki, T., Yoshiike, Y., Sahara, N., and Takashima, A. (2008) *PLoS ONE* **3,** e3540
22. Maeda, S., Sahara, N., Saito, Y., Murayama, S., Ikai, A., and Takashima, A. (2006) *Neurosci. Res.* **54,** 197–201
23. Kimura, T., Yamashita, S., Fukuda, T., Park, J. M., Murayama, M., Mizoroki, T., Yoshiike, Y., Sahara, N., and Takashima, A. (2007) *EMBO J.* **26,** 5143–5152
24. Greenberg, S. G., and Davies, P. (1990) *Proc. Natl. Acad. Sci. U.S.A.* **87,** 5827–5831
25. Götz, J. (2001) *Brain Res. Brain Res. Rev.* **35,** 266–286
26. Alonso Adel, C., Mederlyova, A., Novak, M., Grundke-Iqbal, I., and Iqbal, K. (2004) *J. Biol. Chem.* **279,** 34873–34881
27. von Bergen, M., Barghorn, S., Li, L., Marx, A., Biernat, J., Mandelkow, E. M., and Mandelkow, E. (2001) *J. Biol. Chem.* **276,** 48165–48174
28. Jeganathan, S., Hascher, A., Chinnathambi, S., Biernat, J., Mandelkow, E. M., and Mandelkow, E. (2008) *J. Biol. Chem.* **283,** 32066–32076
29. Shiarli, A. M., Jennings, R., Shi, J., Bailey, K., Davidson, Y., Tian, J., Bigio, E. H., Ghetti, B., Murrell, J. R., Delisle, M. B., Mirra, S., Crain, B., Zolo, P., Arima, K., Iseki, E., Murayama, S., Kretzschmar, H., Neumann, M., Lippa, C., Halliday, G., Mackenzie, J., Khan, N., Ravid, R., Dickson, D., Wszolek, Z., Iwatsubo, T., Pickering-Brown, S. M., and Mann, D. M. (2006) *Neuropathol. Appl. Neurobiol.* **32,** 374–387
30. Agarwal-Mawal, A., and Paudel, H. K. (2001) *J. Biol. Chem.* **276,** 23712–23718
31. Head, E., Lott, I. T., Patterson, D., Doran, E., and Haier, R. J. (2007) *J. Alzheimers Dis.* **11,** 61–76
32. Boekhoorn, K., Terwel, D., Biemans, B., Borghgraef, P., Wiegert, O., Ramakers, G. J., de Vos, K., Krugers, H., Tomiyama, T., Mori, H., Joels, M., van Leuven, F., and Lucassen, P. J. (2006) *J. Neurosci.* **26,** 3514–3523
33. Jeganathan, S., von Bergen, M., Brutlach, H., Steinhoff, H. J., and Mandelkow, E. (2006) *Biochemistry* **45,** 2283–2293

Neurobiology of Disease

Convergence of Presenilin- and Tau-Mediated Pathways on Axonal Trafficking and Neuronal Function

Erica Peethumnongsin,[1,2,3] Li Yang,[1] Verena Kallhoff-Muñoz,[1,4] Lingyun Hu,[5] Akihiko Takashima,[6] Robia G. Pautler,[5] and Hui Zheng[1,2,4]

[1]Huffington Center on Aging, [2]Interdepartmental Program of Cellular and Molecular Biology, [3]Medial Scientist Training Program, [4]Department of Molecular and Human Genetics, and [5]Department of Molecular Physiology and Biophysics, Baylor College of Medicine, Houston, Texas 77030, and [6]Laboratory for Alzheimer's Disease, Brain Science Institute, RIKEN, Saitama 350-0198 3510198, Japan

Alzheimer's disease (AD) is a significant and growing health problem in the aging population. Although definitive mechanisms of pathogenesis remain elusive, genetic and histological clues have implicated the proteins presenilin (PS) and tau as key players in AD development. PS mutations lead to familial AD, and although tau is not mutated in AD, tau pathology is a hallmark of the disease. Axonal transport deficits are a common feature of several neurodegenerative disorders and may represent a point of intersection of PS and tau function. To investigate the contribution of wild-type, as opposed to mutant, tau to axonal transport defects in the context of presenilin loss, we used a mouse model postnatally deficient for PS (PS cDKO) and expressing wild-type human tau (WtTau). The resulting PS cDKO;WtTau mice exhibited early tau pathology and axonal transport deficits that preceded development of these phenotypes in WtTau or PS cDKO mice. These deficits were associated with reduced neurotrophin signaling, defective learning and memory and impaired synaptic plasticity. The combination of these effects accelerated neurodegeneration in PS cDKO;WtTau mice. Our results strongly support a convergent role for PS and tau in axonal transport and neuronal survival and function and implicate their misregulation as a contributor to AD pathogenesis.

Introduction

Alzheimer's disease (AD) is a significant and growing health problem in the aging population. Although definitive mechanisms of pathogenesis remain elusive, genetic and histological clues have implicated the proteins presenilin (PS) and tau as key players in AD development. Studies of familial AD have identified 178 mutations in the *presenilin 1* (*PS1*) gene and 14 mutations in its homolog, *presenilin 2* (*PS2*). Both through its role as the catalytic subunit of γ-secretase and via γ-secretase-independent mechanisms, presenilin can affect multiple cellular systems that mediate neuronal function and survival (for review, see Parks and Curtis, 2007). Unlike presenilin, tau is not known to be mutated in AD. Instead, aberrant phosphorylation of wild-type tau leads to its aggregation into neurofibrillary tangles, a pathological hallmark of AD. This hyperphosphorylation has also been shown to interfere with tau's normal physiological role of binding and stabilizing microtubules, leading to impairments in axonal transport (for review, see Mi and Johnson, 2006).

Received April 16, 2010; revised June 24, 2010; accepted Aug. 4, 2010.

This work was supported by grants from the National Institutes of Health (NIH) (AG20670 and NS40039 to H.Z., and AG29977 to R.G.P.). E.P. was a trainee of NIH Training Grant T32 AG000183. We thank Drs. S. Sisodia (University of Chicago, Chicago, IL) and S. Tonegawa (Massachusetts Institute of Technology, Cambridge, MA) for the *PS1* floxed mice and the CaMKIIα-Cre transgenic line, respectively. We are grateful to N. Aithmitti and X. Chen for expert technical support and members of the Zheng laboratory for constructive discussions. We acknowledge C. Spencer and the Baylor College of Medicine Intellectual and Developmental Disabilities Research Center Neurobehavioral Core (HD24064) for their assistance.

Correspondence should be addressed to Hui Zheng, Huffington Center on Aging, Baylor College of Medicine, One Baylor Plaza, Houston, TX 77030. E-mail: huiz@bcm.edu.

DOI:10.1523/JNEUROSCI.1964-10.2010

 0270-6474/10/3013409-10$15.00/0

Defective axonal transport has been demonstrated in multiple neurodegenerative diseases, including AD, Huntington's disease, and Parkinson's disease (for review, see Higuchi et al., 2002). Tau and presenilin have both been implicated in decreased trafficking in AD, suggesting a common pathway toward neurodegeneration. Loss of presenilin *in vitro* and expression of *PS1* familial AD mutations *in vivo* impair fast axonal transport through dysregulation of GSK3β, a prominent tau kinase that also phosphorylates the motor protein kinesin to promote its release of cargo vesicles (Pigino et al., 2003; Lazarov et al., 2007). Transgenic mouse models of a human tauopathy also exhibit reduced rates of axonal transport (Zhang et al., 2004; Ittner et al., 2008). This phenomenon has been attributed to the propensity of these tau mutants to aggregate into filaments, leading to premature GSK3β-mediated release of kinesin from its cargoes, as with presenilin loss or mutation (LaPointe et al., 2009).

The overlap of presenilin and tau function with regard to axonal transport led us to hypothesize that conditions favoring tau pathology and presenilin loss of function would promote greater inhibition of axonal trafficking through combinatorial effects. We chose presenilin conditional double knock-out (PS cDKO) mice to study postnatal effects of complete presenilin loss to avoid the confounding effects of residual PS function in mutant models (Feng et al., 2004). These mice develop forebrain-specific knock-out of *PS1* on a $PS2^{-/-}$ background, thus preventing PS2 compensation. We bred these animals with mice neuronally expressing 4-repeat human tau (WtTau), which is considered the most pathology-prone of the 6 wild-type human isoforms (Kimura et al., 2007). The resulting PS cDKO;WtTau

mice exhibited early tau pathology and axonal transport deficits that preceded development of these phenotypes in WtTau or PS cDKO mice. These deficits were associated with reduced neurotrophin signaling, defective learning and memory, impaired synaptic plasticity, and accelerated neurodegeneration.

Materials and Methods

Mouse models. All mice in this study were on a C57BL/6J background and were homozygous for both the exon 4-floxed *PS1* allele ($PS1^{fl}$) described by Feng et al. (2001) and the conventional *PS2* knock-out described by Donoviel et al. (1999). These mice have been previously compared with nontransgenic animals and were phenotypically wild-type in all experiments performed; they are therefore considered equivalent to wild-type controls in this study (Feng et al., 2004). Transgenic mice expressing the longest isoform of human tau (WtTau) and CaMKIIα-Cre mice have been described previously (Tsien et al., 1996; Kimura et al., 2007). All genotypes in this study were generated by breeding Cre; $PS1^{fl/fl}$; $PS2^{-/-}$ mice with WtTau; $PS1^{fl/fl}$; $PS2^{-/-}$ mice to yield the following: $PS1^{fl/fl}$; $PS2^{-/-}$ (PS2 KO), $PS1^{fl/fl}$; $PS2^{-/-}$; WtTau (WtTau), Cre; $PS1^{fl/fl}$; $PS2^{-/-}$ (PS cDKO), and Cre; $PS1^{fl/fl}$; $PS2^{-/-}$; WtTau (PS cDKO; WtTau). Mice were housed 2–5 per cage with *ad libitum* access to food and water in a room with a 12 h light/dark cycle. All procedures were performed in accordance with NIH guidelines and with the approval of the Baylor College of Medicine Institutional Animal Care and Use Committee.

Histology and immunohistochemistry. Mice anesthetized with Avertin (2,2,2-tribromoethanol in 2-methyl-2-butanol, 0.4 mg/kg, i.p., Sigma) underwent transcardial perfusion with PBS containing heparin (10 U/ml) and fixation with 4% paraformaldehyde (PFA) for 5 min. Brains (n = 3/genotype) were dissected and postfixed in 30% sucrose in 4% PFA overnight, then transferred to 30% sucrose in PBS, all at 4°C. Frozen brains were sliced into 30 μm floating sections using a sliding microtome (Leica SM2000R) and stored in cryoprotectant solution (0.1 M PBS, pH 7.2, containing 30% sucrose, 30% ethylene glycol, and 1% polyvinylpyrrolidone) at −20°C until further use. For tau immunostaining, endogenous peroxidase activity was blocked and tissue was permeabilized with 3% hydrogen peroxide in Tris-buffered saline (TBS) with 0.5% Triton X-100 for 30 min at room temperature (RT). Sections were then blocked in 5% nonfat dry milk in TBS with 0.4% Triton X-100 for 1 h at RT, then incubated in primary antibody (CP13, 1:5000; MC1, 1:200; generous gifts from Dr. Peter Davies, Albert Einstein College of Medicine, New York, NY) in the milk blocking solution at 4°C overnight. After four 5 min washes with TBS with 0.05% Triton X-100, sections were incubated in biotinylated goat anti-mouse secondary antibody (1:1000, Vector Labs) in 20% Superblock (Pierce Protein Research Products, Thermo Fischer Scientific) in TBS with 0.05% Triton X-100 for 2 h at RT. Sections were again washed 4 × 5 min with TBS with 0.05% Triton X-100, then incubated in avidin-biotin-horseradish peroxidase complex (ABC) reagent (R.T.U. Vectastain Universal Elite ABC kit, Vector Labs, PK-7200) for 1 h at RT. After three 5 min washes with TBS with 0.05% Triton X-100, staining was visualized by incubation in diaminobenzidine (DAB) with hydrogen peroxide (DAB Substrate Kit for Peroxidase, Vector Labs, SK-4100) at RT for 2 min. Sections were then transferred to TBS, mounted onto slides, and then dried overnight before coverslip mounting. Images were acquired on a Zeiss Axioskop 2 Plus upright microscope with Axio Cam MRC camera using Axiovision 3.1 software. For Nissl staining, frozen brain sections were first mounted onto gelatin-coated slides and dried overnight. The tissue was dehydrated by serial passage through 70%, 95%, and 100% ethanol and lipids were removed by immersion in xylene. Sections were then rehydrated and incubated in 0.1% cresyl violet at room temperature for 10 min, followed by a water rinse and differentiation in 95% ethanol until desired staining was observed. Stained tissue was dehydrated in 100% ethanol and cleared by xylene before mounting coverslips with DPX mounting medium (Sigma). Images were acquired on an Olympus IX50 inverted microscope with Photometrics CoolSNAP ES camera using MetaMorph 6.0 software.

Manganese-enhanced magnetic resonance imaging. The use of manganese-enhanced magnetic resonance imaging (MEMRI) to measure *in vivo* axonal transport has been described previously (Smith et al., 2007). Mn^{2+} was administered by nasal lavage of 4 μl (2 μl per nostril) of 0.75 g/ml $MnCl_2$ solution to a mouse anesthetized by 5% isoflurane. The mouse was then allowed to recover for 45 min on a heating pad. Following the recovery period, the mouse was again anesthetized with 5% isoflurane before placement in the prone position in a modified Bruker mouse holder. From this point through imaging, the mouse was maintained on 2–3% isoflurane in 100% O_2; appropriate isoflurane levels were determined by respiration rate (target: 40–60 breaths/min). Respiration rate was measured by a pressure pad placed beneath the animal, and temperature was monitored using a rectal probe. Temperature was maintained at 37°C throughout imaging using an air heating system (SA Instruments). A 9.4T, Bruker Avance Biospec Spectrometer, 21 cm bore horizontal scanner with a 35 mm volume resonator was used for all image acquisition described in this article. For MEMRI experiments, imaging parameters were as follows: repetition time (TR) = 500 ms; echo time (TE) = 10.2 ms; field of view (FOV) = 3.0 cm; slice thickness = 1 mm; matrix = 128 × 128; number of excitations = 2; number of cycles = 15. All images were acquired, and MEMRI images were analyzed, using Paravision software, version 4 (Bruker). Two different cohorts were imaged at 2 months (PS2 KO n = 5, WtTau n = 4, PS cDKO n = 6, PS cDKO;WtTau n = 6) and 6 months (PS2 KO n = 7, WtTau n = 6, PS cDKO n = 7, PS cDKO;WtTau n = 9).

To calculate transport rates, a region of interest (ROI) was designated exactly as in Smith et al. (2007). The ROI was located in an axial slice 1 mm anterior to the posterior aspect of the olfactory bulb. Exact placement was determined by identifying the vertical midpoint of the olfactory bulb and positioning the ROI at this height at the bulb's periphery; this region contains the olfactory neuronal layer at its widest point. The ROI therefore represents a single fascicle of axons originating from olfactory sensory neurons in the nasal epithelium (Akins and Greer, 2006). To normalize for overall changes in signal intensity between images, the signal intensity of this ROI was normalized to a separate, larger ROI within the facial muscle. Normalized signal intensity was then measured for each cycle and the values plotted against time. The axonal transport rate was calculated as the slope of the resulting regression line, and data for each genotype were represented as the mean ± SEM. Data were compared between genotypes by one-way ANOVA with Newman–Keuls posttests using Prism software, version 4 (GraphPad Software).

Synaptosome fractionation. To isolate synaptosome fractions, fresh mouse hippocampi were homogenized in ice-cold buffer (0.32 M sucrose in 10 mM HEPES-NaOH, pH 7.4) containing Complete Protease Inhibitor Cocktail (Roche Diagnostics) with a glass-Teflon homogenizer (10 strokes at 900 rpm). The homogenate was then centrifuged at 4°C in a JA-20 rotor (Beckman-Coulter) at 2500 rpm for 30 min. The resulting supernatant was recentrifuged at 7600 rpm for 30 min to yield a crude synaptosome pellet. This pellet was then resuspended in ice-cold homogenization buffer and lysed hypo-osmotically with 5 mM HEPES, pH 7.4, containing Complete Protease Inhibitor Cocktail. The resuspended synaptosomes were then homogenized with 10 strokes of a glass-Teflon homogenizer at 900 rpm and shaken for 15 min at 4°C. The lysed synaptosomes were then pelleted by centrifugation at 4°C in a JA-17 rotor (Beckman-Coulter) at 10,000 rpm for 30 min and stored at −80°C for future use.

Western blot analysis. For analysis of synaptosome fractions (n = 3/genotype), pellets were resuspended in homogenization buffer. For all other immunoblotting experiments (n = 4/genotype), samples were prepared from quick-frozen hippocampus by homogenization in ice-cold modified RIPA buffer (50 mM Tris, pH 7.4; 150 mM NaCl; 1% NP-40; 1 mM EDTA; 0.25% sodium deoxycholate) with phosphatase and protease inhibitors. Following 3 × 10 pulses of sonication, homogenates were centrifuged at 10,500 × g for 10 min at 4°C and supernatants collected. Protein concentrations of all samples were determined using a detergent-compatible (DC) colorimetric protein assay (Bio-Rad) before dilution in 2× loading buffer. Samples were boiled at 95°C for 5 min before loading. Sample loading was as follows: 5 μg/well for synaptosome quality control Western blots; 15 μg/well for BDNF and CaMKII synaptosome Western blots; 35 μg/well for c-Myc and APPc Western blots; and 50 μg/well for Erk, Akt, and total BDNF and CaMKII Western blots. For BDNF West-

ern blots, samples were run on a 12% SDS-polyacrylamide gel at 100 mV for 2 h; all other proteins were resolved on a 9% gel under the same conditions. Proteins were transferred onto a nitrocellulose membrane (Bio-Rad) in transfer buffer (0.05 M Tris, 0.04 M glycine, 20% methanol, 0.01% SDS) for 1 h at a constant 100 mV, with current between 150 and 200 mA. BDNF membranes were blocked in 5% nonfat dry milk in Superblock overnight at 4°C. All other membranes were blocked in 5% nonfat dry milk in 0.1% Tween 20 (Sigma) in TBS (TBST) for 1 h at room temperature. Membranes were incubated in primary antibody in blocking solution overnight at 4°C. The following antibodies were used: PHF-1, 1:500 (a generous gift from Dr. Peter Davies, Albert Einstein College of Medicine, New York), AT8, 1:500 (Pierce Endogen, Thermo Fisher Scientific), Tau 5, 1:1000 (Millipore Bioscience Research Reagents), γ-tubulin 1:10,000 (Sigma), APPc 1:2000 (Sigma), c-Myc (9E10) 1:1000 (Santa Cruz Biotechnology), BDNF (N-20) 1:500 (Santa Cruz Biotechnology), synaptotagmin 1:500 (a generous gift from Dr. Louis Reichardt, University of California, San Francisco, School of Medicine, San Francisco, CA), NMDAR1, 1:5000 (Millipore Bioscience Research Reagents), Erk1/2, 1:1000 (Cell Signaling Technology), phospho-Erk1/2 (Thr202/Tyr204) 1:1000 (Cell Signaling Technology), Akt 1:1000 (Cell Signaling Technology), phospho-Akt 1:1000 (Cell Signaling Technology), CaMKII 1:500 (Santa Cruz Biotechnology). Following primary incubation, membranes were washed 3 × 10 min with TBST, then incubated in species-specific goat secondary antibody (1:5000, horseradish peroxidase-conjugated anti-mouse or anti-rabbit, Vector Labs) in blocking solution. Membranes were again washed 3 × 10 min with TBST, then bands were visualized using ECL chemiluminescence reagent (GE Healthcare Life Sciences). Band density was calculated using Scion Image software. Band densities normalized to the respective loading controls were then compared with data for PS2 KO mice and represented as percentage of control ± SEM. Data were compared between genotypes by one-way ANOVA with Newman–Keuls posttests using Prism software, version 4 (GraphPad Software).

Associative fear conditioning. PS2 KO ($n = 14$), WtTau ($n = 14$), PS cDKO ($n = 11$), and PS cDKO;WtTau ($n = 16$) male and female mice were tested at 6 months of age. Testing was performed as in Spencer et al. (2006), with the exception that freezing was measured automatically using the FreezeFrame/FreezeView monitoring system (San Diego Instruments) to control testing parameters and collect freezing data with baseline thresholds set just above the level of motion detected in an empty chamber. Training began with a 2 min exploration period in the test chamber (reported as "immediate freezing"), followed by two pairings of conditioned stimulus (CS) (30 s of 80 db white noise) and unconditioned stimulus (US) (2 s 0.7 mA foot shock) separated by 2 min. Twenty-four hours after training, mice were placed back in the training chamber for 5 min to test contextual memory. One hour after context testing, cued memory was tested by introducing the mice for 3 min to the training chamber after visual, tactile, and olfactory conditions were altered, then playing the CS for 3 min. The cued response was reported as the difference between freezing during the CS and freezing during the acclimation period. Datasets for immediate freezing, context freezing, and cued freezing were analyzed separately by one-way ANOVA with Newman–Keuls posttests using Prism software, version 4 (GraphPad Software).

Slice preparation and field EPSP recordings. Horizontal hippocampal slices (400 μm) were prepared from 6- to 7-month-old PS2 KO [$n = 13$ for long-term potentiation (LTP), 30 for paired-pulse], PS cDKO ($n = 14$ for LTP, 21 for paired-pulse), and PS cDKO;WtTau ($n = 11$ for LTP, 32 for paired-pulse) mice using a vibratome (Global Medical Instrumentation, series 1000) and ice-cold cutting artificial CSF (aCSF) containing the following (in mM): 110 sucrose, 60 NaCl, 3 KCl, 7 MgCl, 28 $NaHCO_3$, 1.25 NaH_2PO_4, 5 D-glucose, 0.5 $CaCl_2$. Slices were incubated for 1 h in room-temperature recording aCSF (in mM): 125 NaCl, 2.5 KCl, 1 MgCl, 25 $NaHCO_3$, 1.25 NaH_2PO_4, 10 D-glucose, 2 $CaCl_2$ consistently bubbled with 95%O_2/5%CO_2. Slices were equilibrated for 20–30 min in recording aCSF, at 31 ± 0.5°C before electrode (2–4 mΩ, filled with recording aCSF) placement in area CA1. Schaffer collaterals were stimulated by a bipolar electrode. Basal synaptic transmission was monitored at 0.05 Hz. In paired-pulse experiments, field EPSPs (fEPSPs) were elicited by two-pulse stimulation with interpulse intervals ranged from 10 to 200 ms. Facilitation was evaluated by calculating the ratio P2/P1: where P2 is the fEPSP amplitude elicited by the second stimulus and P1 is the fEPSP amplitude elicited by the first stimulus. Hippocampal LTP was induced using a theta burst protocol (TBS) consisting of 10 bursts at 5 Hz, and each burst consisting of four pulses at 100 Hz, with a pulse width of 0.05 ms. Stimulation strength was set to provide fEPSPs with an amplitude of ~30% of the maximum. fEPSPs were filtered at 2 kHz, digitized at 20 kHz, recorded with Clampex 9 and analyzed with Clampfit software (Molecular Devices) and OriginPro 7.5 (OriginLab).

Three-dimensional magnetic resonance imaging. Equipment and mouse handling were as described in the MEMRI experiments. PS2 KO, PS cDKO, and PS cDKO;WtTau mice were imaged at 2 months (PS2 KO $n = 3$, PS cDKO $n = 2$, PS cDKO;WtTau $n = 2$) and 6 months (PS2 KO $n = 3$, PS cDKO $n = 4$, PS cDKO;WtTau $n = 2$). Images were acquired using a 3D rapid acquisition with relaxed enhancement (RARE) protocol using the following parameters: RARE factor = 8; TR = 2000 ms; TE = 45.2 ms; FOV = 30 mm × 30 mm × 30 mm; matrix size = 128 × 128 × 128; number of averages = 2. Brain regions (cerebral cortex, ventricles, and cerebellum) were manually labeled within each slice and volumes were analyzed using AMIRA software (Mercury Computer Systems) (Redwine et al., 2003). Volumes for each region were compared separately across genotypes by one-way ANOVA with Newman–Keuls posttests using Prism software, version 4 (GraphPad Software).

Results

Loss of presenilin leads to increased tau phosphorylation and pathological conformation changes in both the dentate gyrus and septal nuclei of mice expressing wild-type human tau

Presenilin conditional double knock-out (PS cDKO) mice exhibit tau hyperphosphorylation as early as 9 months of age, a finding that likely results from loss of presenilin's inhibition of certain tau kinases (Saura et al., 2004). We chose to explore this phenotype further by breeding PS cDKO mice with mice expressing the longest isoform of wild-type human tau (WtTau), which serves as a better substrate for aberrant phosphorylation than endogenous mouse tau. The littermate *PS2* knock-out animals produced from the crosses (the details of which can be found in Materials and Methods) were used as controls. These mice have been previously compared with nontransgenic animals and were phenotypically wild-type in all experiments performed; they are therefore considered equivalent to wild-type in this study (Feng et al., 2004). We used immunoblotting to confirm expression of c-Myc-tagged WtTau and accumulation of the C-terminal fragment (CTF) of the amyloid precursor protein (APP), which indicates loss of γ-secretase function. WtTau expression and APP CTF accumulation were observed in their corresponding genotypes within the olfactory bulb, hippocampus, and cortex but were absent in the cerebellum, all of which indicate successful forebrain targeting of genetic modifications in PS and tau (supplemental Fig. S1, available at www.jneurosci.org as supplemental material). We hypothesized that these PS cDKO;WtTau mice would develop tau pathology earlier than PS2 single knock-out (PS2 KO), WtTau, and PS cDKO controls. As predicted, while control genotypes did not exhibit tau hyperphosphorylation by 6 months of age, PS cDKO;WtTau mice demonstrated pathological alterations in tau in certain brain regions. Using the CP13 antibody to detect phosphorylation of serine 202 and MC-1 to detect pretangle conformational changes in tau, we observed distinct immunoreactivity with both antibodies in the polymorphic and granule cell layers of the dentate gyrus of the hippocampus in these mice (Fig. 1*A*). The lateral and medial septal nuclei also exhibited a high number of CP13- and MC-1-positive neurons (Fig. 1*B*). Both antibodies characteristically stained the somatodendritic compartments of the neurons, indicating pathological

localization of tau (Fig. 1*A*,*B*, high magnification). The recognition of these neurons by MC-1 also reflects pathological changes in tau conformation as seen in human AD brains. These findings were specific to the hippocampus, as the striatum and cortex did not display CP13- or MC-1-positive neurons in any of the genotypes tested (supplemental Figure S2, available at www.jneurosci.org as supplemental material).

Western blotting of dissected hippocampus from 6-month-old mice revealed an increase in immunoreactivity for AT8, which recognizes phosphorylation of serine 202 and threonine 205, and PHF-1, which detects phosphorylated serine 396 and 404, in PS cDKO;WtTau animals (Fig. 1*C*). Similar experiments performed in dissected septum did not reveal differences between genotypes, most likely due to the small number of CP13- and MC-1-positive neurons in that area (data not shown). The AT8 results corroborate our findings that CP13 immunoreactivity, and therefore ser202 phosphorylation, is increased in the dentate gyrus of these mice. Increased PHF-1 site phosphorylation suggests a progression toward paired-helical filament development and represents the furthest degree of tau pathology detected in our studies. Consistent with this assessment, Campbell-Switzer silver stain did not reveal any neurofibrillary tangles in any of the genotypes at this age (data not shown), indicating that late-stage pathology is not yet present.

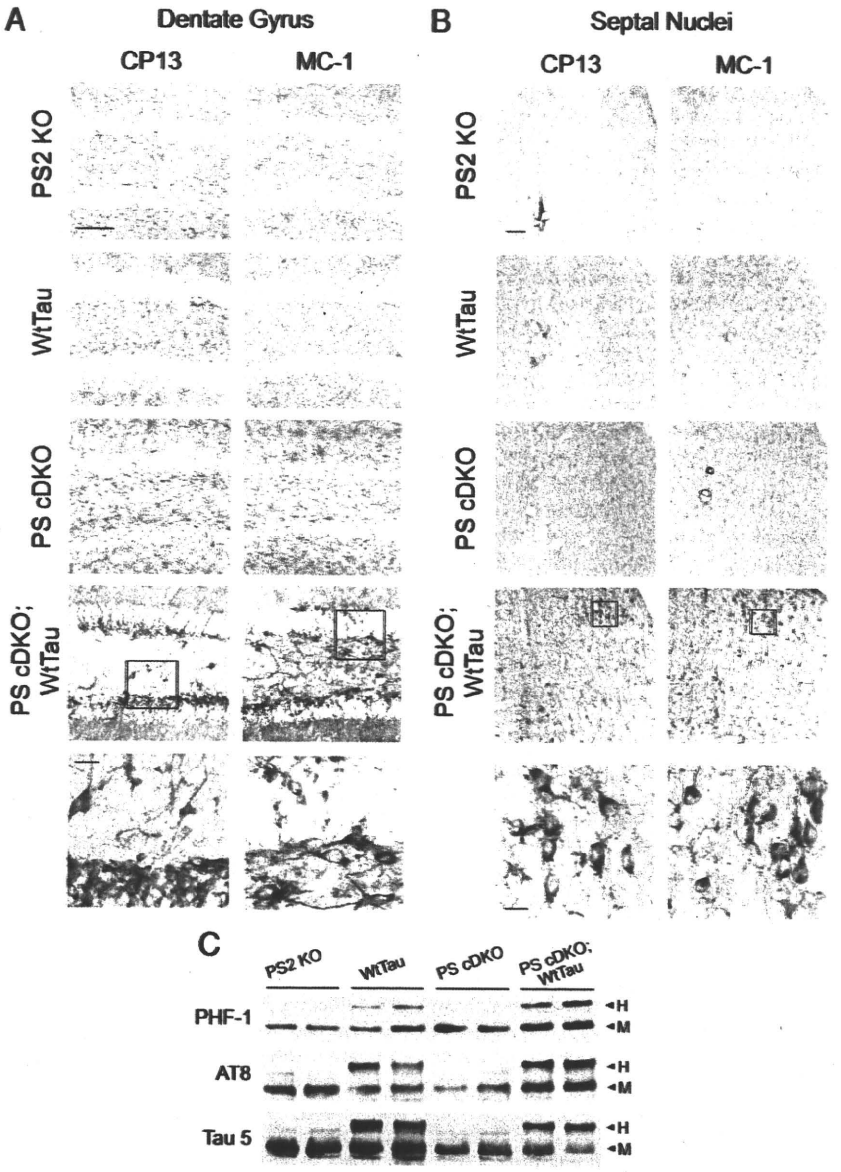

Figure 1. Tau pathology in 6-month-old PS cDKO;WtTau mice. ***A***, Representative images from the dentate gyrus showing CP13 (left) and MC-1 (right) immunostaining of PS2 KO, WtTau, PS cDKO, and PS cDKO;WtTau mice. ***B***, Representative images of CP13 and MC-1 immunostaining of a region including both the dorsolateral septal nucleus (upper right of each panel) and the medial septum (lower left of each panel). High-magnification insets show characteristic somatodendritic immunoreactivity in PS cDKO; WtTau neurons. Scale bars, 10 μm for inset images, 50 μm for all others. ***C***, Representative Western blots of phosphorylated (PHF-1 and AT8) and total (Tau 5) tau in hippocampal tissue homogenates dissected from 6-month-old mice show increased tau phosphorylation in PS cDKO;WtTau animals. H, human transgenic tau; M, mouse endogenous tau.

The expression of WtTau in PS cDKO mice leads to a reduction in anterograde axonal transport rates

Because tau hyperphosphorylation can impair axonal trafficking, we used Mn^{2+}-enhanced magnetic resonance imaging (MEMRI) to measure the efficiency of fast axonal transport. This method takes advantage of multiple useful features of manganese: 1) Mn^{2+} ions are paramagnetic and thus can serve as contrast agents for MRI; 2) as a calcium (Ca^{2+}) analog, Mn^{2+} exploits the cellular machinery responsible for uptake and vesicular packaging of Ca^{2+} to be effectively introduced to the neuron and its transport system; and 3) Mn^{2+} moves anterogradely along microtubules via fast axonal transport, allowing measurements of its synaptic accumulation to reflect overall transport rates (Mendonça-Dias et al., 1983; Burnett et al., 1984; Geraldes et al., 1986; Cory et al., 1987; Fornasiero et al., 1987; Sloot and Gramsbergen, 1994; Tindemans et al., 2003; Cross et al., 2008; Minoshima and Cross, 2008). We chose to measure trafficking in the olfactory system because it provides a convenient and pathologically relevant site for measurement of Mn^{2+} transport; ions can be administered noninvasively via nasal lavage and olfactory deficits have been well documented in patients with Alzheimer's disease (Mesholam et al., 1998; Peters et al., 2003).

Figure 2*A* shows representative images from 6-month-old PS2 KO and PS cDKO;WtTau mice at the first and last time points with outlined areas emphasizing signal enhancement. We tested PS2 KO, WtTau, PS cDKO, and PS cDKO;WtTau mice at 2 and 6 months of age and found that mice of all genotypes exhibited normal rates of transport at the younger age, indicating that the system is not developmentally impaired (Fig. 2*B*). At 6 months, however, PS cDKO;WtTau mice displayed a reduction ($\sim$50%, $p < 0.001$) in the rate of axonal transport compared with controls (Fig. 2*C*). This reduced rate was remarkably consistent between PS cDKO;WtTau animals (Fig. 2*D*). Interestingly, neither WtTau nor PS cDKO mice showed deficits at this age, providing evidence for a genetic interaction between presenilin and tau.

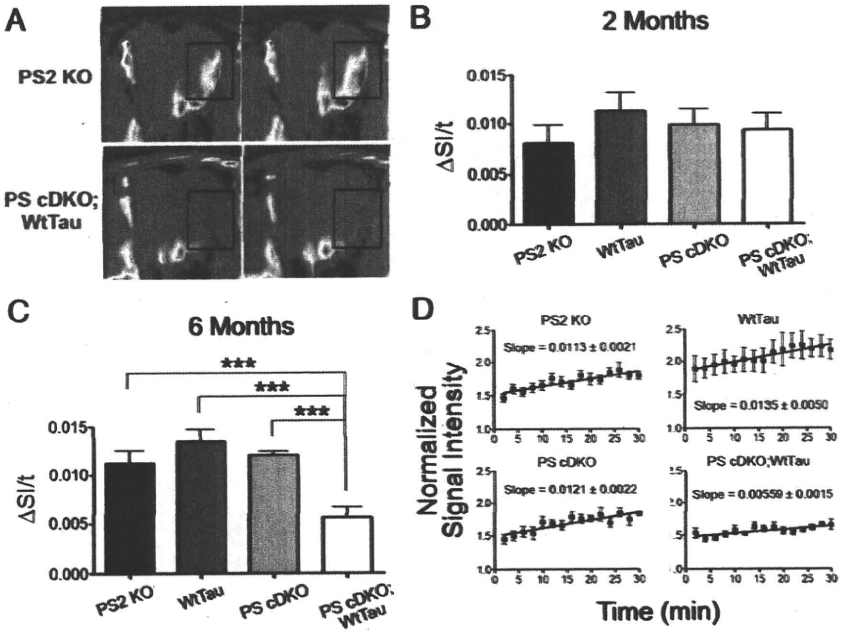

Figure 2. Age-dependent reduction in axonal transport rates of PS cDKO;WtTau mice. ***A***, Representative MEMRI color map images from PS2 KO controls and PS cDKO;WtTau mice at 6 months of age showing signal enhancement (emphasized by rectangular outline) between the first image (left) and the last image (right) of the series. ***B***, Axonal transport rates are normal in 2-month-old PS2 KO, WtTau, PS cDKO, and PS cDKO;WtTau mice. ***C***, Axonal transport rates at 6 months are selectively reduced in PS cDKO;WtTau mice. ***D***, Linear regression of all data points from each genotype of 6-month-old mice. Given slopes are graphically represented and statistically analyzed in ***C***). $\Delta SI/t$ = change in normalized signal intensity over time = rate of axonal transport. $^{***}p < 0.001$.

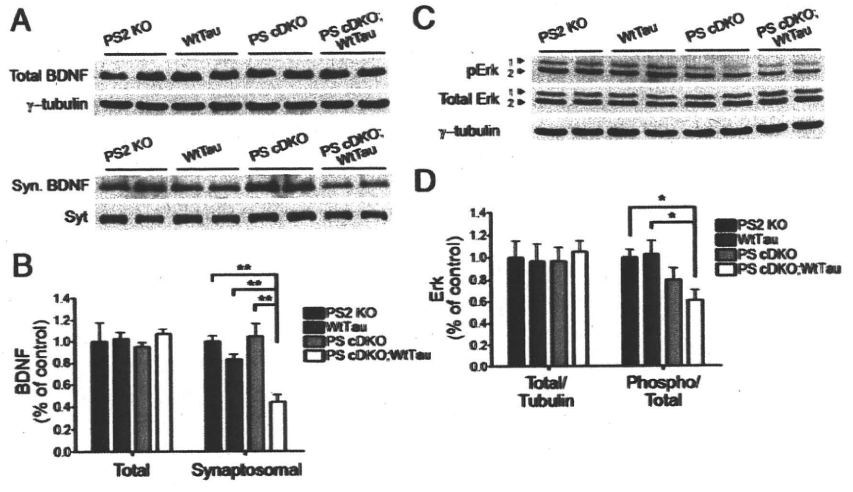

Figure 3. Decreased synaptosomal BDNF levels and Erk1/2 activation in the hippocampus of 6-month-old PS cDKO;WtTau animals. ***A***, Representative Western blots of total BDNF and BDNF from synaptosome fractions (BDNF). ***B***, Quantification of normalized BDNF band densities relative to control (PS2 KO). ***C***, Representative Western blots of total and phospho-Erk1/2. ***D***, Quantification of normalized Erk1/2 band densities relative to control. Loading controls were as follows: synaptotagmin (Syt) for synaptosomal BDNF and γ-tubulin for all others. $^{*}p < 0.05$, $^{**}p < 0.01$.

PS cDKO;WtTau mice exhibit reductions in synaptic brain-derived neurotrophic factor levels and Erk activation

To investigate the consequences of decreased axonal transport, we next examined brain-derived neurotrophic factor (BDNF) levels in the hippocampus. BDNF synthesis and anterograde trafficking occur within the hippocampus, but some hippocampal BDNF is also received anterogradely from the entorhinal cortex (Conner et al., 1997; Caleo and Cenni, 2004). BDNF is reduced in the brains of patients with AD, and recent work has shown that administration of BDNF into the entorhinal cortex can improve cell signaling, cognition, and neuronal survival in various mammalian models of AD through transport and signaling to the hippocampus (Murer et al., 2001; Gauthier et al., 2004; Nagahara et al., 2009). We therefore sought to determine whether the observed axonal transport deficit in PS cDKO;WtTau mice would cause a decrease in BDNF trafficking to the hippocampus, thus impairing its downstream signaling. Although total BDNF levels were unchanged in the hippocampi of PS2 KO, WtTau, PS cDKO, and PS cDKO;WtTau mice at 6 months of age, synaptosomal BDNF was decreased in PS cDKO;WtTau mice (Fig. 3*A*,*B*, $p < 0.01$), indicating a reduction in localization of BDNF to the synapse. Synaptotagmin undergoes anterograde transport through a mechanism distinct from that of BDNF and therefore served as both a loading control for the synaptosome fraction and a separate confirmation of the specific change in BDNF synaptic localization. The quality of synaptosomal fractionation was determined by Western blots for enrichment of the synaptic proteins PSD-95 and NMDA receptor 1 (supplemental Fig. S3, available at www.jneurosci.org as supplemental material).

BDNF binds to its receptor, Tropomycin-related kinase B (TrkB), at the synapse to initiate downstream signaling through three main pathways: the phosphatidylinositol 3-kinase (PI3K)-Akt pathway, the phospholipase Cγ1 (PCγ1)-Ca^{2+} pathway, and the Ras-mitogen-activated protein kinase (MAPK)-Erk1/2 pathway (Kaplan and Miller, 2000). Total levels of Erk were unchanged in all genotypes at 6 months of age, but activation of Erk through phosphorylation was specifically reduced in PS cDKO; WtTau mice (Fig. 3*C*,*D*, $p < 0.05$). Preliminary immunoblotting experiments did not detect changes in expression or activation of certain members of the PI3K or PCγ1 pathways (supplemental Fig. S4, available at www.jneurosci.org as supplemental material), but the possibility of altered signaling cannot be excluded. These data suggest that impaired transport of BDNF to the synapse leads to reduced downstream signaling through Erk.

Additional expression of WtTau worsens contextual memory deficits in PS cDKO mice at 6 months of age

Because of Erk's well established role in learning and memory, we used the conditioned fear paradigm to test associative memory in 6-month-old mice. Impairments in contextual memory have been reported in PS cDKO mice as early as 2 months of age, and cued learning deficits have also been observed in these animals at 12 months of age (Saura et al., 2004; Chen et al., 2008). The

percentage of time the mice spent frozen during the initial phase of training, before exposure to conditioned and unconditioned stimuli, was unchanged across genotypes, suggesting that baseline activity and anxiety levels were similar in all tested animals (Fig. 4*A*, Immediate). Consistent with previous studies, we observed a significant decrease (~40%, $p < 0.01$) in freezing of PS cDKO mice during the context test, reflecting a defect in hippocampus-dependent associative memory. Interestingly, PS cDKO;WtTau mice exhibited an even larger impairment in contextual memory (~65%, $p < 0.001$ vs control), which was significantly worse than that of PS cDKO animals (Fig. 4*A*, Context Test, $p < 0.05$ vs PS cDKO). We did not detect a difference in freezing of 6-month-old mice of any genotype during the cued test, indicating that amygdala-mediated learning pathways were functioning properly and that contextual memory deficits were likely due to hippocampus-specific defects (Fig. 4*A*, Cued Test).

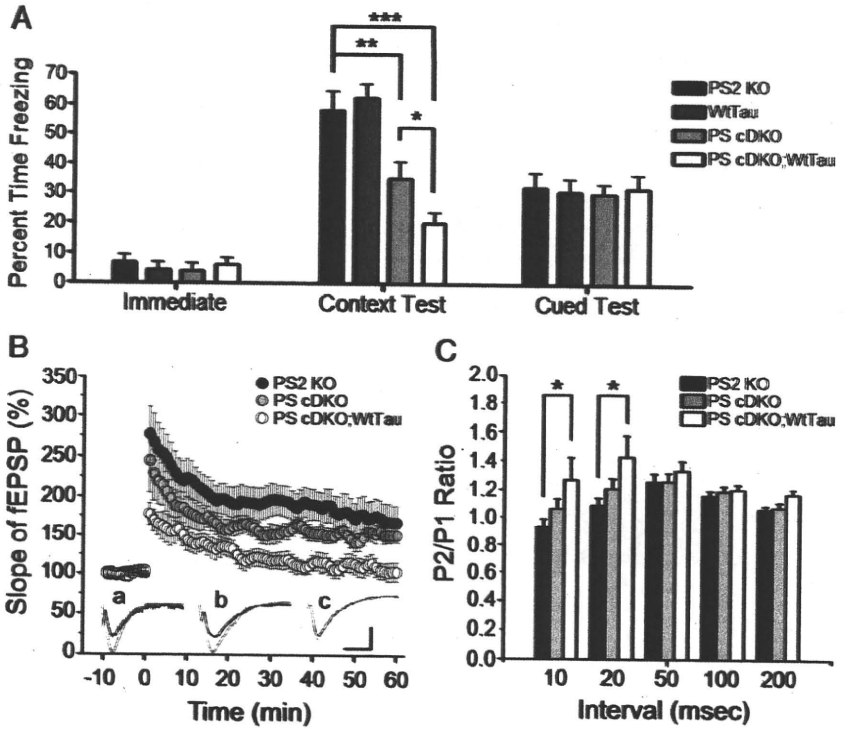

Figure 4. Hippocampal-dependent memory and synaptic plasticity impairments in PS cDKO;WtTau mice at 6 months of age. ***A***, Freezing behaviors during various phases of fear conditioning. Immediate freezing occurs during the initial exploratory period of training. Context test freezing represents the amount of time the mice froze during second exposure to the training chamber 24 h after training. Normalized cued test freezing is the difference between freezing during second exposure to the conditioned stimulus (CS) and freezing before CS in a novel chamber 24 h after training. ***B***, Following 10 min of baseline recording, theta burst stimulation (TBS) was delivered to the Schaffer collateral pathway. When compared with PS2 KO controls, PS cDKO;WtTau mice demonstrate significantly impaired LTP induction and maintenance at all time points tested; however, the difference between PS cDKO;WtTau and PS cDKO mice reaches significance only at the initial 3 and last 40 min. No significant difference is observed between PS cDKO and PS2 KO mice. Insets (***a–c***), Example fEPSP traces taken before and after TBS from PS2 KO, PS cDKO, and PS cDKO;WtTau mice, respectively (calibration, 1 mV, 5 ms). ***C***, Increased paired-pulse ratio in PS cDKO;WtTau mice at 10 and 20 ms interpulse intervals indicating altered presynaptic function in the hippocampus of PS cDKO;WtTau mice. $*p < 0.05$, $**p < 0.01$, $***p < 0.001$.

Presynaptic alteration underlies impaired Schaffer collateral LTP in PS cDKO;WtTau mice

In addition to being important modulators of learning and memory, BDNF and Erk play critical roles in LTP (Ying et al., 2002). We therefore examined field Schaffer collateral LTP in hippocampal brain slices of 6-month-old PS2 KO, PS cDKO and PS cDKO;WtTau mice. Potentiation induced by theta-burst stimulation (TBS) was significantly reduced and remained lower in PS cDKO;WtTau mice compared with PS2 KO controls ($p < 0.01$), but we found no significant differences between PS cDKO and PS2 KO animals (Fig. 4*B*). In contrast, the difference in LTP induction and maintenance between PS cDKO;WtTau and PS cDKO mice only reached significance during the first three and last 40 min ($p < 0.05$). To determine whether the deficit in LTP was related to presynaptic or postsynaptic defects, we conducted a paired-pulse protocol in which the ratio between the mean amplitudes of the second fEPSP over the first fEPSP (P2/P1 ratio) is inversely related to the initial release probability (Dobrunz and Stevens, 1997). In general, the smaller the probability of release to the first pulse, the more facilitated the response to the second pulse. We observed a significantly increased paired-pulse ratio in PS cDKO;WtTau mice compared with PS2 KO controls at the shortest interpulse intervals tested (Fig. 4*C*, $p < 0.05$), suggesting a reduced initial release probability in the PS cDKO;WtTau animals. Thus, altered presynaptic function may underlie the impaired Schaffer collateral LTP observed in PS cDKO;WtTau mice.

Expression of WtTau exacerbates cortical neurodegeneration in PS cDKO mice

PS cDKO mice are known to exhibit atrophy of the cerebral cortex by 6 months of age (Feng et al., 2004; Saura et al., 2004; Chen et al., 2008). Given our findings that the addition of WtTau can impair axonal transport, neurotrophin signaling, contextual memory, and LTP in PS cDKO mice, we hypothesized that these deficits could impact neuronal survival in this mouse model with proven susceptibility to cellular insults. We chose three-dimensional magnetic resonance imaging (3D MRI) to evaluate neurodegeneration because this method presents an opportunity to measure the volume of entire brain regions *in vivo*, eliminating the inconsistencies associated with histological processing. While our primary region of interest was the cerebral cortex, we also looked for the compensatory enlargement of ventricles that accompanies loss of cortical tissue. The volume of the cerebellum was analyzed as a negative control. Because no neuronal loss has been observed in WtTau mice up to 22 months of age, we elected to omit this group (Kimura et al., 2007). The other three genotypes were studied at 2 months of age to control for developmental differences in brain volumes and at 6 months to determine whether the aforementioned impairments at this age have an effect on neuron loss.

As expected, the volumes of all brain regions were comparable across genotypes at 2 months of age, demonstrating normal brain development in the absence of postnatal presenilin expression (Fig. 5*A*). As previously reported, PS cDKO mice exhibited a reduction in cortical volume at 6 months of age, which was accompanied by a compensatory increase in ventricular volume (Fig. 5*B*). Interestingly, PS cDKO;WtTau mice displayed even greater cortical atrophy at this age, supporting a role for tau in

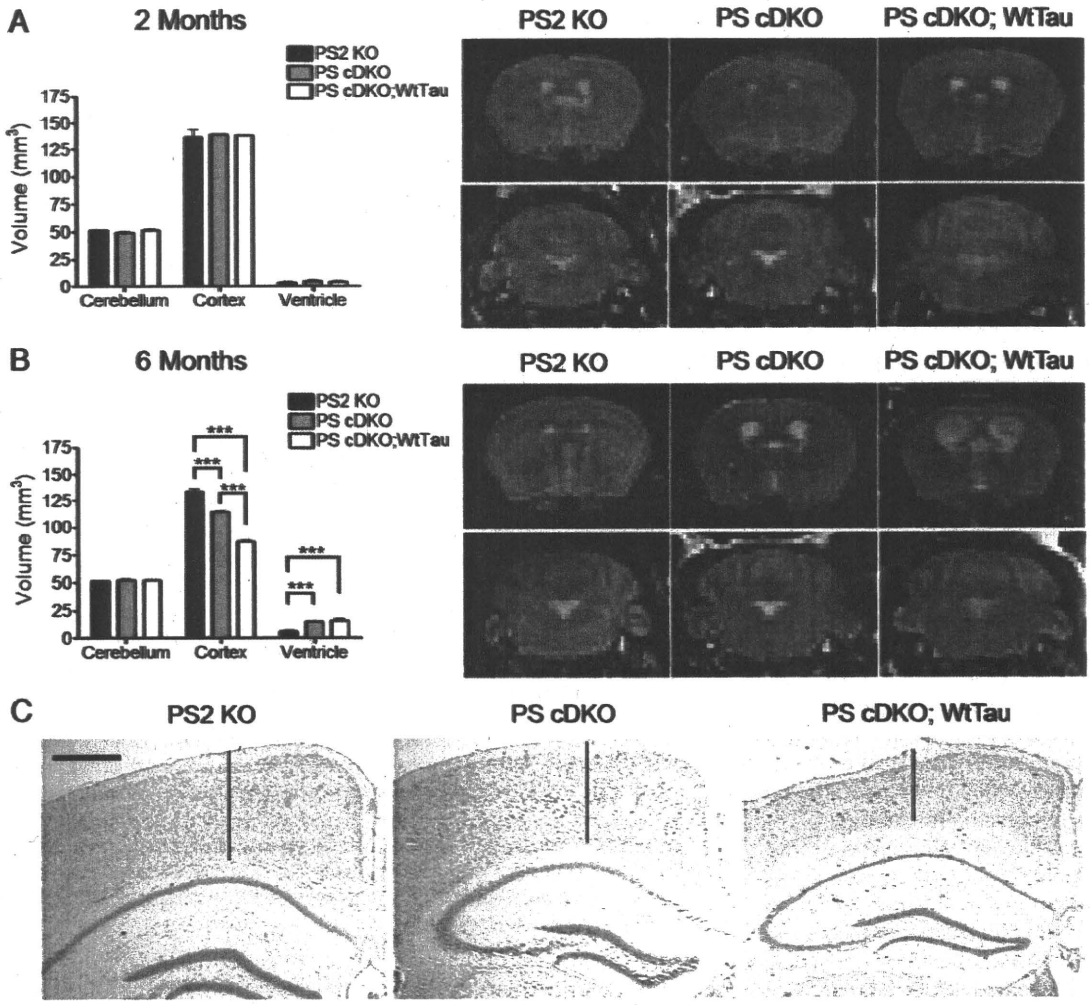

Figure 5. Increased cortical neurodegeneration in PS cDKO;WtTau compared with PS cDKO mice. ***A***, Volumes of cerebellum, cerebral cortex, and ventricles are normal in 2-month-old PS2 KO, PS cDKO, and PS cDKO;WtTau mice. Quantification of volumes (left) and representative 3D MRI images (right) show no obvious differences in structures between genotypes. ***B***, Cerebral cortical atrophy of PS cDKO mice is exacerbated in PS cDKO;WtTau animals at 6 months. Quantification of volumes (left) and representative 3D MRI images (right) show a decrease in cortical volume with compensatory increase in ventricular volume (top) in PS cDKO mice and, to a further degree, in PS cDKO;WtTau mice. No change in cerebellar volumes was detected (bottom). ***C***, Representative images from cresyl violet (Nissl)-stained frozen brain sections demonstrate cortical atrophy in 6-month-old PS cDKO and PS cDKO;WtTau mice as quantified in panel 5B. Vertical lines are provided to assist with visual assessment of cortical thickness at sites that are comparable between sections. Scale bar, 500 μm, $^{***}p < 0.001$.

this neurodegenerative phenotype (Fig. 5*B*,*C*). At both ages, cerebellar volumes remained stable across genotypes, indicating that changes in cortical and ventricular volumes resulted specifically from the CaMKIIα-regulated genetic modifications in PS cDKO and PS cDKO;WtTau mice.

Discussion

Although a large body of evidence supports some level of interaction between presenilin and tau in AD pathogenesis, the precise contributions of each have yet to be fully ascertained. Specifically, the role of wild-type human tau has been largely passed over in favor of study of mutant tau-expressing mouse models, which more readily develop tau pathology but do not accurately reflect the genetics of tau in AD. Here we have shown that expression of WtTau in PS cDKO mice can impair multiple cellular functions that are significant to the development of AD (Fig. 6). In these mice, tau hyperphosphorylation and pathological conformation were detected as early as 6 months of age in neurons of the septal nuclei of the basal forebrain and the dentate gyrus of the hippocampus. We determined that anterograde axonal transport was impaired specifically in PS cDKO;WtTau mice at this time point, suggesting a role for tau hyperphosphorylation and/or aggregation in this deficit. In the hippocampus, reduced synaptosomal BDNF in the context of normal levels of total BDNF provided additional support for the hypothesis that axonal transport is impaired in areas with tau pathology. The finding that Erk activation was also diminished in the hippocampus of PS cDKO;WtTau mice implied that this level of synaptic BDNF reduction was sufficient to decrease its downstream signaling. Deficient BDNF/Erk signaling had important consequences for contextual learning and memory, and long-term potentiation as well, as impairments in both were observed to a greater degree in PS cDKO mice expressing WtTau. Finally, the combination of these deficits led to an increase in cortical atrophy in PS cDKO;WtTau mice when compared with PS cDKO mice, suggesting that multiple mechanisms underlie the neurodegeneration in these mice, and possibly in AD.

The presence of tau pathology in the septal nuclei and dentate gyrus of PS cDKO;WtTau mice could have several implications for neuronal function in the hippocampus. Septal neurons are

known to project to the dentate gyrus in addition to other hippocampal and extrahippocampal regions. Lesion of septal cholinergic neurons or pharmacological inhibition of septohippocampal cholinergic signaling impairs hippocampal-dependent learning and memory, a deficit that can be rescued by administration of acetylcholine to the hippocampus (for review, see Parent and Baxter, 2004). This corresponds with the loss of cholinergic neurons in AD, which results in memory impairment that can be partially allayed by treatment with acetylcholinesterase inhibitors (Kása et al., 1997; Seltzer, 2006). In addition, pharmacological inhibition of cholinergic signaling by scopolamine has been shown to reduce protein levels of BDNF in the rodent hippocampus (Kotani et al., 2006). Although we did not detect a change in total levels of BDNF in the hippocampus, tau phosphorylation of a subset of neurons in the septohippocampal pathway would perturb the system to a significantlys lesser degree than global inhibition of cholinergic signaling. This limited tau phosphorylation also explains our inability to detect with Western blots the tau pathology observed with immunohistochemistry. Ultimately, the finding that interruption of cholinergic signaling can lead to reductions in downstream BDNF levels provides support for our model that disruption of septohippocampal signaling through tau hyperphosphorylation leads to reduced synaptic BDNF in the hippocampus. Furthermore, strong involvement of this pathway in hippocampal-dependent learning and memory implies a potential mechanism for the specific contextual memory deficit we observed in PS cDKO;WtTau mice.

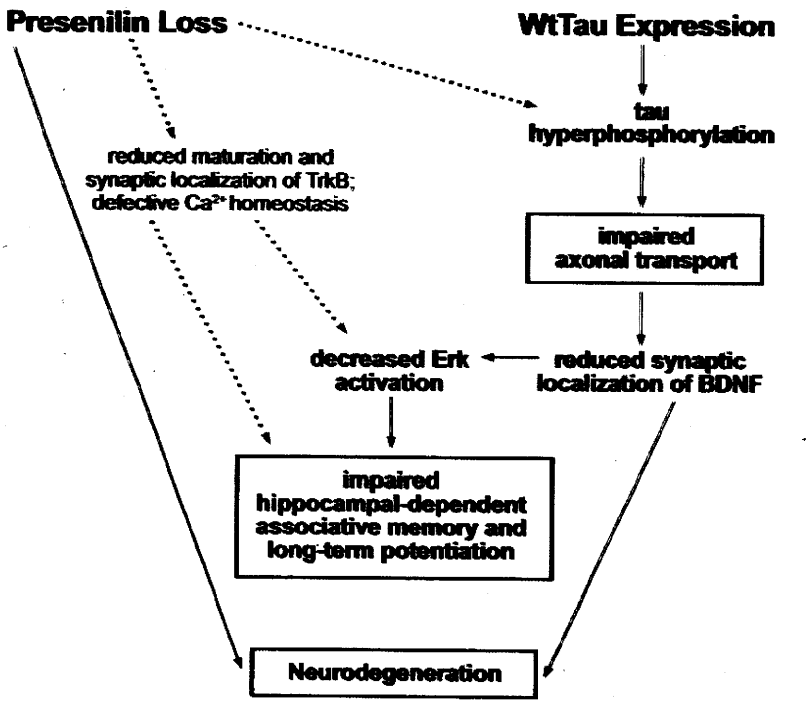

Figure 6. Model of neuronal dysfunction and neurodegeneration in PS cDKO;WtTau mice. Presenilin loss has been shown previously to increase tau phosphorylation, reduce TrkB receptor maturation and synaptic localization, and result in defective Ca^{2+} homeostasis (dotted lines; see Discussion for references). In combination with presenilin loss, expression of WtTau accelerates tau hyperphosphorylation, leading to impaired anterograde axonal transport of synaptic proteins such as BDNF. This decrease in BDNF at the synapse reduces downstream signaling, which, along with loss of presenilin, can directly affect neuronal survival. In addition, specific reduction of Erk phosphorylation/activation impairs hippocampal-dependent memory and long-term potentiation, phenotypes to which presenilin loss likely contributes through mechanisms outside the scope of this study. Boxed results were obtained from *in vivo* studies, with the exception of LTP.

The development of tau pathology and impaired axonal transport in PS cDKO;WtTau mice are likely mediated by changes in the activity of tau kinases. Levels of p25, a potent activator of the tau kinase Cdk5, have been shown to increase in PS cDKO mice by 9 months of age (Saura et al., 2004). Interestingly, loss of presenilin has also been shown to increase GSK3β kinase activity, leading to GSK3β-mediated phosphorylation of the motor protein kinesin to promote its release from its membrane-bound cargoes during anterograde axonal transport (Morfini et al., 2002; Pigino et al., 2003). GSK3β misregulation due to presenilin loss could also lead to tau phosphorylation, suggesting two possible mechanisms for kinase-mediated axonal transport defects in PS cDKO mice: directly through kinesin phosphorylation, and/or indirectly through tau phosphorylation. Because PS cDKO mice did not demonstrate impairment of axonal transport in our studies, tau phosphorylation appears to exert a more profound effect on trafficking than kinesin phosphorylation. Other kinases that phosphorylate tau could also be involved, and it is possible that a combination of small increases in multiple kinases, rather than large increases in a single kinase's activity, could be responsible for the tau phenotypes observed in our study.

While most neurotrophins undergo primarily retrograde axonal transport from the synapse to the cell body, anterograde transport of BDNF is seen in multiple pathways within the brain, including septal and cortical projections to the hippocampus and intrahippocampal circuits (for review, see Schindowski et al., 2008). Along with our observation that synaptic localization of BDNF is reduced, this supports the hypothesis that the defects in axonal transport detected in the olfactory system of PS cDKO; WtTau mice might extend to other brain regions, notably the hippocampus. Decreased Erk signaling in the hippocampus and functional deficits in hippocampal-dependent memory and synaptic plasticity in PS cDKO;WtTau animals further support this notion. In addition to a role for impaired axonal transport in reduced BDNF/Erk signaling, presenilin loss may contribute to this phenotype through other mechanisms. Loss of presenilin in primary neurons results in decreased maturation and membrane localization of TrkB, the primary receptor for BDNF (Naruse et al., 1998). This reduction in mature TrkB at the synaptic membrane could exacerbate an Erk signaling impairment caused by reduced synaptic BDNF. Although PS cDKO mice did not exhibit a statistically significant reduction in Erk activation, a downward trend was observed in these mice, supporting the existence of more than one mechanism underlying this phenotype. In fact, this could be the case with each of the phenotypes exhibited by PS cDKO mice that were exacerbated in PS cDKO;WtTau animals (i.e., contextual memory deficits and neurodegeneration).

Although LTP defects were not clearly demonstrated in PS cDKO mice, a trend toward reduced potentiation did exist. As with Erk signaling, other effects of presenilin loss could be contributing to this phenotype. LTP and other measures of synaptic plasticity require Ca^{2+} signaling, which is regulated by presenilin and is defective in familial AD mutants or PS-deficient mice (for